

Using kinematic boundary lines for particle mass measurements and disambiguation in SUSY-like events with missing energy

Michael Burns, Konstantin T. Matchev, Myeonghun Park

Physics Department, University of Florida, Gainesville, FL 32611, USA

ABSTRACT: We revisit the method of kinematical endpoints for particle mass determination, applied to the popular SUSY decay chain $\tilde{q} \rightarrow \tilde{\chi}_2^0 \rightarrow \tilde{\ell} \rightarrow \tilde{\chi}_1^0$. We analyze the uniqueness of the solutions for the mass spectrum in terms of the measured endpoints in the observable invariant mass distributions. We provide simple analytical inversion formulas for the masses in terms of the measured endpoints. We show that in a sizable portion of the SUSY mass parameter space the solutions always suffer from a two-fold ambiguity, due to the fact that the original relations between the masses and the endpoints are piecewise-defined functions. The ambiguity persists even in the ideal case of a perfect detector and infinite statistics. We delineate the corresponding dangerous regions of parameter space and identify the sets of “twin” mass spectra. In order to resolve the ambiguity, we propose a generalization of the endpoint method, from single-variable distributions to two-variable distributions. In particular, we study analytically the boundaries of the $\{m_{j\ell(lo)}, m_{j\ell(hi)}\}$ and $\{m_{\ell\ell}, m_{j\ell\ell}\}$ distributions and prove that their shapes are in principle sufficient to resolve the ambiguity in the mass determination. We identify several additional independent measurements which can be obtained from the boundary lines of these bivariate distributions. The purely kinematical nature of our method makes it generally applicable to any model that exhibits a SUSY-like cascade decay.

KEYWORDS: Hadronic Colliders, Beyond Standard Model, Supersymmetry Phenomenology.

Contents

1. Introduction	1
2. Analytical results	8
2.1 Forward formulas	9
2.1.1 On-shell scenario	9
2.1.2 Off-shell scenario	10
2.2 Inversion formulas	12
3. Duplication analysis	14
4. Kinematic boundary lines for the $m_{jl(lo)}^2$ versus $m_{jl(hi)}^2$ distribution	22
5. Kinematic boundary lines for the m_{ll}^2 vs. m_{jl}^2 distribution	31
6. Summary and outlook	37
A. Appendix: Simple inversion formulas in regions \mathcal{R}_1, \mathcal{R}_2 and \mathcal{R}_3	40

1. Introduction

The dark matter problem of astroparticle physics [1] greatly motivates the search for neutral, stable and weakly interacting massive particles (WIMPs) at colliders [2]. WIMPs are also rather ubiquitous in Beyond Standard Model (BSM) physics at the TeV scale. Unfortunately, at the hadron colliders of the current energy frontier (the Fermilab Tevatron and the Large Hadron Collider (LHC) at CERN), the process of *direct* WIMP production, tagged with a jet or a photon from initial state radiation, suffers from insurmountable backgrounds [3–5]. In contrast, the chances of a discovery are typically greatly enhanced in case of *indirect* production, where the WIMPs are produced in the decays of heavier, more strongly interacting particles.

Since the WIMPs are usually stable due to some new conserved quantum number, they cannot be singly produced in collisions of light SM particles. The prototypical WIMP example is the lightest superpartner (LSP) (typically the lightest neutralino $\tilde{\chi}_1^0$) in low-energy supersymmetry (SUSY) with R -parity conservation [6]¹. The superpartners are produced in pairs and each one decays through a cascade decay chain down to the $\tilde{\chi}_1^0$ WIMP, which does

¹More recently, it was realized that many of the features of R -parity conserving SUSY are also shared by other model frameworks, such as Universal Extra Dimensions (UED) [7–9], Warped Extra Dimensions [10–12], Little Higgs theory with T -parity [13, 14], etc.

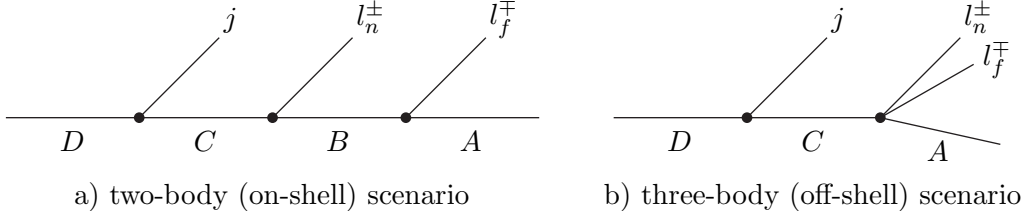


Figure 1: The generic decay chain considered in this paper: $D \rightarrow jC \rightarrow jl_n^\pm B \rightarrow jl_n^\pm l_f^\mp A$. Particles A , B , C and D are new BSM particles, while the corresponding SM decay products consist of a jet j , a “near” lepton l_n^\pm and a “far” lepton l_f^\mp . a) In the two-body (on-shell) scenario, C is kinematically allowed to decay to B , which then decays to A . b) In the three-body (off-shell) scenario, C is kinematically prohibited to decay to B , and decays directly to A .

not interact in the detector and can only manifest itself as missing energy (MET). Since each event contains two unobserved WIMPs (with unknown mass), measuring the masses, spins, etc. of the new particles is a very challenging task. In recognition of this fact, in recent years there has been an increased interest in developing new techniques for mass [15–58] and spin [59–81] measurements in such SUSY-like missing energy events.

There are three basic types of mass determination methods, which are reviewed and contrasted in Ref. [56]. In this paper we concentrate on the classic method of kinematical endpoints [15]. Following the previous SUSY studies, for illustration of our results we shall use the generic decay chain $D \rightarrow jC \rightarrow jl_n^\pm B \rightarrow jl_n^\pm l_f^\mp A$ shown in Fig. 1. Here A , B , C and D are heavy BSM particles, while the corresponding SM decay products are: a QCD jet j , a “near” lepton l_n^\pm and a “far” lepton l_f^\mp . This chain is quite common in SUSY, with the identification $D = \tilde{q}$, $C = \tilde{\chi}_2^0$, $B = \tilde{l}$ and $A = \tilde{\chi}_1^0$, where \tilde{q} is a squark, \tilde{l} is a slepton, and $\tilde{\chi}_1^0$ ($\tilde{\chi}_2^0$) is the first (second) lightest neutralino. However, our analysis is not limited to SUSY, since the decay chain in Fig. 1 is rather typical for other BSM models as well, e.g. UED [9]. For completeness, we shall consider the two different cases shown in Figs. 1(a) and 1(b), correspondingly. In Fig. 1(a) $m_B < m_C$, so that the $C \rightarrow l_n^\pm B$ decay is two-body. In what follows, we shall refer to this case as the “two-body” or “on-shell” scenario. On the other hand, in Fig. 1(b) $m_B > m_C$ and the decay $C \rightarrow l_n^\pm l_f^\mp A$ is three-body, leading to a “three-body” or “off-shell” scenario [33]. In the two-body scenario, the goal is to determine all four unknown masses, m_D , m_C , m_B , and m_A . In the three-body scenario, the goal is to determine the three² unknown masses, m_D , m_C , and m_A . Of course, the scenario is not known until the data are examined, thus an additional goal of our analysis will be to identify the particular scenario at hand.

The idea of the kinematic endpoint method is very simple. Given the SM decay products exhibited in Fig. 1, form the invariant mass³ of every possible combination, m_{ll} , m_{jl_n} , m_{jl_f} ,

²In the three-body scenario of Fig. 1(b), it may still be possible to extract the fourth mass m_B from the data, e.g. by analyzing the shapes of the invariant mass distributions [28]. However, those approaches are quite challenging, since the shapes depend on a number of additional factors: the experimental resolution, the spins of the new particles, the shape of the underlying backgrounds, etc. In contrast, here we are concentrating on methods which use only kinematic endpoint information and are thus immune to those detrimental factors.

³We shall see below that the formulas simplify if we consider invariant masses *squared* instead. This

and m_{jll} . Since l_n^\pm and l_f^\mp cannot be distinguished on an event-by-event basis, one has to introduce an alternative definition of the jl distributions. For example, one can identify the two leptons by their charge and consider the samples $\{jl^+\}$ and $\{jl^-\}$, which are experimentally well defined. This approach turned out to be very useful for spin studies [59, 61, 67, 80], since spin effects are encoded in the *difference* between those two distributions. However, for mass determination, it is more suitable to use an m_{jl} ordering by invariant mass:

$$m_{jl(lo)} \equiv \min \{m_{jl_n}, m_{jl_f}\}, \quad (1.1)$$

$$m_{jl(hi)} \equiv \max \{m_{jl_n}, m_{jl_f}\}. \quad (1.2)$$

Both of the newly defined quantities $m_{jl(lo)}$ and $m_{jl(hi)}$ also exhibit upper kinematic endpoints ($m_{jl(lo)}^{\max}$ and $m_{jl(hi)}^{\max}$, correspondingly), which are experimentally measurable. Together with the measured kinematic endpoints m_{ll}^{\max} and m_{jll}^{\max} of the m_{ll} and m_{jll} distributions, this gives 4 measurements

$$m_{ll}^{\max}, m_{jll}^{\max}, m_{jl(lo)}^{\max}, m_{jl(hi)}^{\max}, \quad (1.3)$$

which are known functions⁴ of only 4 unknown parameters (m_A , m_B , m_C and m_D). Therefore, by inverting those relations, i.e. solving the so called “inverse problem” at the LHC [82], one would expect to be able to determine the complete spectrum, at least as a matter of principle.

However, this determination can be ambiguous, and several alternative solutions for the masses may emerge, as already recognized in, for example [26, 82–89]. This may happen for one of the following reasons.

1. *Insufficient number of measurements.* The four measurements (1.3) may not all be independent from each other. Indeed, there are certain regions of parameter space (reviewed explicitly below in Sec. 2.1) where one finds the following correlation [26]

$$(m_{jll}^{\max})^2 = \left(m_{jl(hi)}^{\max}\right)^2 + (m_{ll}^{\max})^2. \quad (1.4)$$

In this case, the four measurements (1.3) are clearly insufficient and one has to supplement them with an additional measurement. To this end, it has been suggested to consider the constrained distribution $m_{jll(\theta > \frac{\pi}{2})}$, which exhibits a useful *lower* kinematic endpoint $m_{jll(\theta > \frac{\pi}{2})}^{\min}$ [21]. The distribution $m_{jll(\theta > \frac{\pi}{2})}$ is nothing but the usual m_{jll} distribution over a subset of the original events, subject to the additional dilepton mass constraint

$$\frac{m_{ll}^{\max}}{\sqrt{2}} < m_{ll} < m_{ll}^{\max}. \quad (1.5)$$

In the rest frame of particle B , this cut implies the following restriction on the opening angle θ between the two leptons [20]

$$\theta > \frac{\pi}{2}, \quad (1.6)$$

distinction is not central to our analysis.

⁴See Section 2.1 below.

thus justifying the notation for $m_{jll(\theta>\frac{\pi}{2})}$. In what follows, we shall therefore always supplement the original set of 4 measurements (1.3) with the additional measurement of $m_{jll(\theta>\frac{\pi}{2})}^{min}$:

$$m_{ll}^{max}, m_{jll}^{max}, m_{jl(lo)}^{max}, m_{jl(hi)}^{max}, m_{jll(\theta>\frac{\pi}{2})}^{min}, \quad (1.7)$$

so that in principle there is sufficient information to determine the four unknown masses. Then, we shall concentrate on the question whether this determination is unique or not, i.e. we shall be concerned only with discrete ambiguities. As discussed in more detail below in Sections 2 and 3, these discrete ambiguities arise due to the very nature of the mathematical problem: the relations giving the endpoints in terms of the masses are *piecewise-defined* functions, i.e. their definitions depend on the values of the independent variables (the masses m_A , m_B , m_C and m_D). Since the masses are unknown, it is not clear which definition is the relevant one, and one must consider all possibilities, obtain each solution, and test for consistency at the very end.

2. *Experimental resolution.* Ideally, the procedure just described would yield a single consistent solution. Indeed, this is what happens throughout a large portion of the parameter space. One should keep in mind that the measurements (1.7) inevitably come with some experimental errors, so that within those experimental uncertainties, two or more solutions are possible [26, 27, 83]. One specific example of this type is shown in Table 1 for the SPS1a(α) mass spectrum, which was extensively studied in [26]. Even with 300 fb^{-1} of data at the LHC, the residual experimental uncertainties (due to the finite detector resolution, statistical and systematic errors, etc.) will still allow two solutions: a “true” and a “false” one, as shown in the table. However, this is not a true ambiguity in the sense that it arises simply due to limitations in the experimental precision. With time, the latter would be expected to improve and the ambiguity may eventually get resolved. For example, the statistical errors would be reduced with even more data⁵.
3. *Non-uniqueness of the inversion.* Even in the ideal case of a perfect experiment, which would yield results for all the five measurements (1.7) with zero error bars, there may still be multiple solutions to the inversion problem. One of the main goals of this paper is to identify the specific circumstances when this takes place. In Section 3 we shall analyze the physical mass parameter space of SUSY and find a sizable portion in it where an *exact* duplication occurs, i.e. if Nature chooses a SUSY spectrum from that region, the measurements (1.7) will be consistent with two and only two SUSY mass spectra: the nominal one, plus a “fake”. We emphasize the fact that the duplicate solutions we find yield mathematically *identical* values for *all five* experimental observables in (1.7). Therefore, neither improvements in the experimental resolution, nor increased statistics

⁵It is also worth noting that ref. [26] conservatively assigned a rather large systematic error for the $m_{jll(\theta>\frac{\pi}{2})}^{min}$ measurement, since the analytical shape of its edge was unknown at the time. Since then, the shape was derived in [32], so that by now the threshold measurement $m_{jll(\theta>\frac{\pi}{2})}^{min}$ should be considered on equal footing with the other measurements in (1.7).

Variable	SPS1a(α) [26,83]			SU1 [84]		SU3 [84]	
	Nominal	True	False	True	False	True	False
$m_{\tilde{\chi}_1^0}$	96.1	96.3	85.3	137.0	122.1	118.0	346.8
$m_{\tilde{l}_R}$	143.0	143.2	130.4	254.0	127.5	155.0	411.1
$m_{\tilde{\chi}_2^0}$	176.8	177.0	165.5	264.0	245.9	219.0	451.6
$m_{\tilde{q}_L}$	537.2	537.5	523.5	760.0	743.6	631.0	899.9
Region	(1,1)	(1,1)	(1,2)	(1,1)	(1,3)	(1,3)	(1,1)
m_{ll}^{max}	77.0	77.0	77.1	61		100	
$m_{jl(lo)}^{max}$	298.3	298.3	299.6	194		322	
$m_{jl(hi)}^{max}$	375.6	375.6	375.7	600		418	
m_{jll}^{max}	425.8	425.8	425.6	609		499	
$m_{jll(\theta>\frac{\pi}{2})}^{min}$	200.6	200.6	205.1	143	148	247	214

Table 1: Examples of “mass ambiguities” previously reported in [26,83,84]. The nominal values for the mass spectrum are given in the leftmost column in each case. The analysis of [26,83] for the SPS1a(α) study point used all five available measurements (1.7), and included detector resolution effects and statistical and systematic errors. As a result, in the case of SPS1a(α) there are two solutions: the “true” one is in the correct region (1,1) and is close to the nominal values, while the “false” one is in the wrong region (1,2), but nevertheless matches all of the observed invariant mass endpoints (1.7) within the experimental uncertainties. The study points SU1 and SU3 are taken from [84], where one requires a perfect match to only the four kinematic endpoints (1.3), ignoring any experimental errors. In this case the true and false spectra predict different values of $m_{jll(\theta>\frac{\pi}{2})}^{min}$.

will be able to resolve this duplication. Several studies in the literature [26,34,83,84] have already raised the issue of a potential ambiguity in the SUSY mass determination. Some representative examples from those works are shown in Table 1. As already mentioned, the duplication found in [26,83] in the case of SPS1a(α) was simply due to the experimental uncertainties, and would be resolved in a perfect experiment. On the other hand, the duplication in the case of SU1 and SU3 found in Ref. [84] is exact, but relies on only four (namely, the set (1.3)) out of the five available measurements (1.7). As seen from Table 1, the inclusion of the threshold $m_{jll(\theta>\frac{\pi}{2})}^{min}$ will in principle resolve the ambiguity. In contrast, we use the full set of measurements (1.7), including $m_{jll(\theta>\frac{\pi}{2})}^{min}$, and we still find exact duplication. In this sense, our findings, first reported in [86,87], are new, and extend the results of [26,34,83,84]. For example, we find that exact duplication occurs in the (2,3), (3,1) and (3,2) parameter space regions (according to the classification in Section 2), while the examples in Table 1 belong to regions (1,1), (1,2) and (1,3). It is also worth pointing out that the duplicated regions of parameter space that we find are *not* consistent with a typical MSUGRA-type scenario, which may explain why this problem has not been more broadly appreciated earlier. Numerical examples of a duplication similar to ours have previously been presented in [82], and

our analytical results below in Section 3 now help understand their origin.

Having identified the problem of duplication in the measured mass spectrum, in the second part of the paper we present a new method for its solution. As already emphasized, the two-fold ambiguity in the spectrum is exact, so it cannot be resolved by simply improving the experimental precision on the kinematical endpoint measurements (1.7). Instead, additional experimental input is needed. One option is to consider a longer decay chain, which would yield several additional endpoint measurements. For example, the decay chains in Fig. 1 may begin with an even heavier particle (say, E), at the expense of a single new parameter (the mass of particle E) [27]. However, the presence of such a decay chain in the data is a model-dependent assumption and is by no means guaranteed. Alternatively, one may supplement (1.7) with data from a future lepton collider [83], but its existence is also an assumption and is by no means guaranteed. Therefore we do not consider these possibilities here.

Instead, we concentrate on the question: What additional information, which is already present in the hadron collider data, can be used to resolve the ambiguity? It is important to realize that in very general terms, the kinematics of the decay in Fig. 1 is governed by some three-dimensional differential distribution

$$\frac{d^3\Gamma}{d\alpha d\beta d\gamma}, \quad (1.8)$$

where α , β and γ are some suitably chosen angles specifying the particular decay configuration (see, e.g. [61]). Through a change of variables, these angles can be traded for three invariant mass combinations of the visible decay products in Fig. 1, e.g. m_{ll}, m_{jl+}, m_{jl-} [69], but other sets are equally possible, let us denote a generic such set by $\{m_1, m_2, m_3\}$. In place of (1.8) one then has

$$\frac{d^3\Gamma}{dm_1 dm_2 dm_3}. \quad (1.9)$$

The distribution (1.9) is experimentally observable and is nothing but a three-dimensional histogram. It contains the full information about the decay in Fig. 1, including the particle mass and spin information. The only disadvantage of (1.9) is that it cannot be easily visualized.

In order to obtain a kinematic endpoint for some mass parameter, say m_1 , one then simply integrates over the other two degrees of freedom, and builds the one-dimensional distribution

$$\frac{d\Gamma}{dm_1} \equiv \int dm_2 dm_3 \frac{d^3\Gamma}{dm_1 dm_2 dm_3}. \quad (1.10)$$

This, being a one-dimensional distribution, exhibits an upper *endpoint* m_1^{max} . However, in the process of integration in (1.10), one is losing a certain amount of the original information contained in (1.9). Some of this information can be recovered if we consider a two-dimensional (bivariate) distribution, e.g. in (m_1, m_2) :

$$\frac{d^2\Gamma}{dm_1 dm_2} \equiv \int dm_3 \frac{d^3\Gamma}{dm_1 dm_2 dm_3}. \quad (1.11)$$

This, being a two-dimensional distribution, will exhibit not an endpoint, but a *boundary line*, which can be parameterized by a single parameter t as $(m_1(t), m_2(t))$. Finally, if we stick to the original three-dimensional distribution (1.9), we will obtain a *boundary surface*, parameterized by two parameters, t_1 and t_2 , as $(m_1(t_1, t_2), m_2(t_1, t_2), m_3(t_1, t_2))$. Given that bivariate and trivariate distributions are more informative than the simple one-dimensional histograms, it is rather surprising that they have not been used more often in the previous analyses of SUSY mass determination.

The second part of the paper is thus devoted to the analysis of bivariate distributions of the type (1.11)⁶. In particular, in Section 4 (Section 5) we analyze the boundaries of the bivariate distributions in terms of $m_{jl(lo)}^2$ and $m_{jl(hi)}^2$ (m_{jl}^2 and m_{ll}^2). We show that the shapes of those distributions are very distinct and can be used to identify qualitatively the type of spectrum at hand, thus resolving the duplication discussed above. We also provide analytical formulas for the boundaries of the kinematically allowed regions, which can be used to further quantitatively improve on the mass determination (see also [89]). Clearly, fitting to a line would yield a better precision of determining the mass parameters than simply fitting to a point. What is more, we shall show that the bivariate distributions offer the possibility of several additional measurements, in addition to those in (1.7). These are the locations of some special points on the boundary lines, for which we provide analytic expressions in terms of the masses m_A , m_B , m_C and m_D . These special points are typically hidden as subtle features of the one-dimensional distributions but are transparent on the bivariate distributions which we are advertising here.

In conclusion of this section, we summarize the main goals and results of this paper and point to the sections where those results can be found.

- *Analytical solution of the inverse problem.* In Section 2.2 we provide analytical formulas which allow one to calculate directly the BSM mass spectrum m_A , m_B , m_C and m_D in terms of the experimental inputs (1.7). Our formulas are completely general, for example, they are valid for both the on-shell scenario of Fig. 1(a) as well as the off-shell scenario of Fig. 1(b). In addition, they can be applied to *all* regions in parameter space. The availability of exact analytical expressions for the mass spectrum in terms of the observed kinematical endpoints makes numerical fitting (e.g. with a program like Fittino [90]) unnecessary. An important simplification in our approach is that we only need to consider four different cases, as opposed to the 11 cases usually discussed in the literature.
- In Section 3 we identify the *complete* SUSY mass parameter space where *exact* duplication occurs, i.e. two very different mass spectra predict identical values for all five endpoint measurements (1.7).
- In Section 4 we analyze the shape of the bivariate distribution in terms of $m_{jl(lo)}^2$ and $m_{jl(hi)}^2$. We identify the characteristic shape of the boundary lines of the distribution

⁶Preliminary results of our work were reported in [85, 87]. Similar ideas were discussed more recently in [88, 89].

for each of our four parameter space regions. The shape not only allows to resolve the ambiguity discovered in Section 3, but also contains a lot of additional useful information. For example, the shape analysis yields an additional measurement of an “edge” point, $m_{jl_f}^{(p)}$, and also allows to determine the endpoints $m_{jl_n}^{\max}$ and $m_{jl_f}^{\max}$ of the underlying m_{jl_n} and m_{jl_f} distributions. The analytic solution to the inverse problem (presented in Appendix A) takes a particularly simple form if we make use of these new measurements and consider the alternative set $\{m_{ll}^{\max}, m_{jl_f}^{(p)}, m_{jl_n}^{\max}, m_{jl_f}^{\max}\}$.

- In Section 5 we perform a similar shape analysis of the bivariate distribution in terms of m_{jl}^2 versus m_{ll}^2 .

2. Analytical results

In this section we present the analytical formulas which allow one to go from the mass spectrum to the experimentally observable endpoints (Sec. 2.1) and vice versa (Sec. 2.2).

Before we begin, we introduce some notation. Following existing studies in the literature [30, 61, 67, 80], we shall redefine the original mass parameter space

$$\{m_A, m_B, m_C, m_D\} \quad (2.1)$$

in terms of an overall squared mass scale, m_D^2 , and squared mass ratios⁷

$$R_{ij} \equiv \frac{m_i^2}{m_j^2}, \quad (2.2)$$

where $i, j \in \{A, B, C, D\}$. Note that there are only three independent squared mass ratios in (2.2), which we shall take as the set $\{R_{AB}, R_{BC}, R_{CD}\}$. However, in what follows we shall also make use of the other ratios, e.g. R_{AC} , R_{AD} and R_{BD} , whenever this will lead to a simplification of our formulas. Of course, the latter are related to our preferred set $\{R_{AB}, R_{BC}, R_{CD}\}$ due to the transitivity property

$$R_{ij}R_{jk} = R_{ik}. \quad (2.3)$$

Notice also the useful identity

$$R_{ij}R_{kl} = R_{il}R_{kj}. \quad (2.4)$$

We also require all of the mass parameters (2.2) to be positive semidefinite. Our analysis assumes three additional absolute conditions on these parameters.

$$R_{AB} < 1, \quad R_{AC} < 1, \quad R_{CD} < 1. \quad (2.5)$$

This imposes a general mass hierarchy,

$$0 < m_A < m_C < m_D, \quad (2.6)$$

⁷The practice of redefining the parameter space in terms of squared mass ratios is quite common in the literature. For example, our variables $\{R_{CD}, R_{BC}, R_{AB}\}$ exactly correspond to the variables $\{x, y, z\}$ used in [61, 67, 80] and the parameters $\{R_C, R_B, R_A\}$ used in [30].

while for the mass of B the only constraint is $m_A < m_B$. Depending on the mass of B , we can obtain either the on-shell scenario of Fig. 1(a), in which $m_A < m_B < m_C$, or the off-shell scenario of Fig. 1(b), in which $m_C < m_B$ and possibly even $m_D < m_B$. In summary, we shall use

$$\{m_D, R_{AB}, R_{BC}, R_{CD}\} \quad (2.7)$$

as our default parametrization of the 4 dimensional mass parameter space (2.1).

2.1 Forward formulas

Here we list the well known formulas for the endpoints (1.7) in terms of the parameters (2.7) introduced above.

2.1.1 On-shell scenario

In the on-shell scenario the kinematical endpoints are given by the following formulas:

$$a \equiv (m_{ll}^{max})^2 = m_D^2 R_{CD} (1 - R_{BC}) (1 - R_{AB}); \quad (2.8)$$

$$b \equiv (m_{jll}^{max})^2 = \begin{cases} m_D^2 (1 - R_{CD}) (1 - R_{AC}), & \text{for } R_{CD} < R_{AC}, \text{ case (1, -),} \\ m_D^2 (1 - R_{BC}) (1 - R_{AB} R_{CD}), & \text{for } R_{BC} < R_{AB} R_{CD}, \text{ case (2, -),} \\ m_D^2 (1 - R_{AB}) (1 - R_{BD}), & \text{for } R_{AB} < R_{BD}, \text{ case (3, -),} \\ m_D^2 (1 - \sqrt{R_{AD}})^2, & \text{otherwise, case (4, -);} \end{cases} \quad (2.9)$$

$$c \equiv (m_{jl(l)}^{max})^2 = \begin{cases} (m_{jl_n}^{max})^2, & \text{for } (2 - R_{AB})^{-1} < R_{BC} < 1, \text{ case (-, 1),} \\ (m_{jl(eq)}^{max})^2, & \text{for } R_{AB} < R_{BC} < (2 - R_{AB})^{-1}, \text{ case (-, 2),} \\ (m_{jl(eq)}^{max})^2, & \text{for } 0 < R_{BC} < R_{AB}, \text{ case (-, 3);} \end{cases} \quad (2.10)$$

$$d \equiv (m_{jl(hi)}^{max})^2 = \begin{cases} (m_{jl_f}^{max})^2, & \text{for } (2 - R_{AB})^{-1} < R_{BC} < 1, \text{ case (-, 1),} \\ (m_{jl_f}^{max})^2, & \text{for } R_{AB} < R_{BC} < (2 - R_{AB})^{-1}, \text{ case (-, 2),} \\ (m_{jl_n}^{max})^2, & \text{for } 0 < R_{BC} < R_{AB}, \text{ case (-, 3);} \end{cases} \quad (2.11)$$

where

$$(m_{jl_n}^{max})^2 = m_D^2 (1 - R_{CD}) (1 - R_{BC}), \quad (2.12)$$

$$(m_{jl_f}^{max})^2 = m_D^2 (1 - R_{CD}) (1 - R_{AB}), \quad (2.13)$$

$$(m_{jl(eq)}^{max})^2 = m_D^2 (1 - R_{CD}) (1 - R_{AB}) (2 - R_{AB})^{-1}. \quad (2.14)$$

The physical meaning of the latter three quantities will become clear in the course of the discussion in Section 4. Finally, the endpoint $m_{jll(\theta>\frac{\pi}{2})}^{min}$ introduced earlier in the Introduction, is given by

$$e \equiv \left(m_{jll(\theta>\frac{\pi}{2})}^{min} \right)^2 = \frac{1}{4} m_D^2 \left\{ (1 - R_{AB})(1 - R_{BC})(1 + R_{CD}) \right. \\ \left. + 2(1 - R_{AC})(1 - R_{CD}) - (1 - R_{CD})\sqrt{(1 + R_{AB})^2(1 + R_{BC})^2 - 16R_{AC}} \right\}. \quad (2.15)$$

The physical meaning of the latter quantity will be revealed in Section 5. In (2.8-2.15) we have introduced some convenient shorthand notation

$$a = (m_{ll}^{max})^2, \quad b = (m_{jll}^{max})^2, \quad c = (m_{jl(lo)}^{max})^2, \quad d = (m_{jl(hi)}^{max})^2, \quad e = (m_{jll(\theta>\frac{\pi}{2})}^{min})^2 \quad (2.16)$$

for the kinematical endpoints of the mass *squared* distributions⁸.

One can see that the formulas (2.9-2.11) are piecewise-defined: they are given in terms of different expressions, depending on the parameter range for R_{AB} , R_{BC} and R_{CD} . This divides the $\{R_{AB}, R_{BC}, R_{CD}\}$ parameter space into several distinct regions, illustrated in Fig. 2. Following [26], we label those by a pair of integers (N_{jll}, N_{jl}) . As already indicated in eqs. (2.9-2.11), the first integer N_{jll} identifies the relevant case for m_{jll}^{max} , while the second integer N_{jl} identifies the corresponding case for $(m_{jl(lo)}^{max}, m_{jl(hi)}^{max})$. In the on-shell case considered here, only 9 out of the 12 pairings (N_{jll}, N_{jl}) are physical, and they are all exhibited within the unit square of Fig. 2. The remaining two regions (5,4) and (6,4) seen in Fig. 2 correspond to the off-shell case and will be introduced below in Sec. 2.1.2. Notice at this point that the formula for the $m_{jll(\theta>\frac{\pi}{2})}^{min}$ threshold is unique.

Using (2.8), (2.9) and (2.11), it is easy to check that the relation (1.4), which can be equivalently rewritten in the new notation as

$$b = a + d, \quad (2.17)$$

is identically satisfied in regions (3,1), (3,2) and (2,3) of Fig. 2. Therefore, in these regions one would necessarily have to rely on the additional information provided by the measurement of the e endpoint (2.15).

2.1.2 Off-shell scenario

We now list the relevant formulas [33] for the off-shell scenario of Fig. 1(b), in which $m_B >$

⁸Note that Ref. [26] uses a, b, c, d to label the same endpoints, but for the *linear* masses instead of the masses squared.

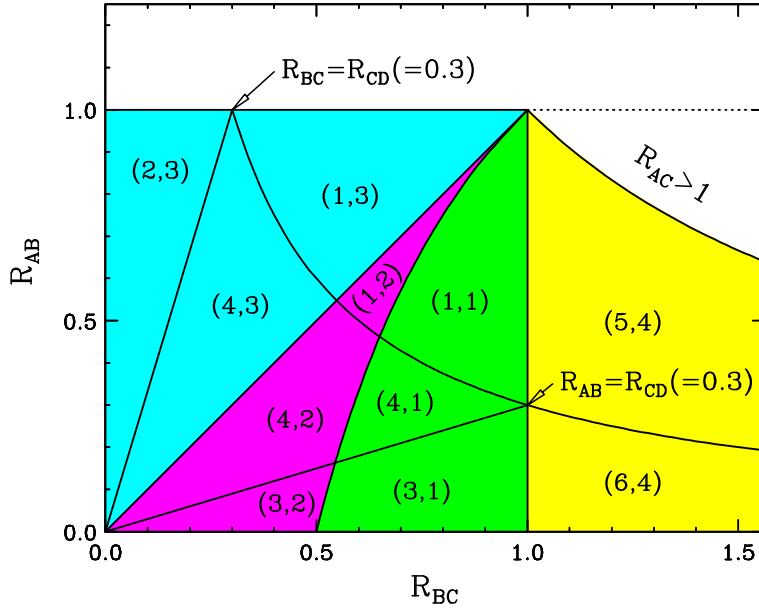


Figure 2: A slice through the $\{R_{AB}, R_{BC}, R_{CD}\}$ parameter space at a fixed $R_{CD} = 0.3$, illustrating the 11 parameter space regions (N_{jl}, N_{ll}) resulting from the piecewise-definition of the m_{jl}^{max} endpoint in eqs. (2.9) and (2.19) and the $(m_{jl}^{max}, m_{jl}^{max})$ endpoints in eqs. (2.10), (2.11), (2.20) and (2.21). The four N_{jl} regions used later in our analysis are color-coded as follows: $N_{jl} = 1$ (green); $N_{jl} = 2$ (magenta); $N_{jl} = 3$ (cyan) and $N_{jl} = 4$ (yellow).

m_C , i.e. $R_{BC} > 1$:

$$a \equiv (m_{ll}^{max})^2 = m_D^2 R_{CD} (1 - \sqrt{R_{AC}})^2; \quad (2.18)$$

$$b \equiv (m_{jl}^{max})^2 = \begin{cases} m_D^2 (1 - R_{CD})(1 - R_{AC}), & \text{for } R_{CD} < R_{AC}, \text{ case } (5, -), \\ m_D^2 (1 - \sqrt{R_{AD}})^2, & \text{otherwise, case } (6, -); \end{cases} \quad (2.19)$$

$$c \equiv \left(m_{jl(l)}^{max}\right)^2 = \frac{1}{2} m_D^2 (1 - R_{CD})(1 - R_{AC}), \quad \text{case } (-, 4); \quad (2.20)$$

$$d \equiv \left(m_{jl(h)}^{max}\right)^2 = m_D^2 (1 - R_{CD})(1 - R_{AC}), \quad \text{case } (-, 4); \quad (2.21)$$

$$e \equiv \left(m_{jl(\theta>\frac{\pi}{2})}^{min}\right)^2 = \frac{1}{4} m_D^2 (1 - \sqrt{R_{AC}}) \left\{ 2R_{CD}(1 - \sqrt{R_{AC}}) \right. \quad (2.22)$$

$$\left. + (1 - R_{CD}) \left(3 + \sqrt{R_{AC}} - \sqrt{1 + R_{AC} + 6\sqrt{R_{AC}}} \right) \right\}.$$

Notice the absence of the B index in these expressions, indicating that they are indeed independent of the mass m_B of the heavy (off-shell) particle B . Nevertheless, the off-shell case can still be represented in the (R_{BC}, R_{AB}) parameter plane of Fig. 2 as the right-

most yellow-shaded region. Its left boundary is the line $R_{BC} = 1$, beyond which particle B becomes on shell, while its upper boundary is the line $R_{AB}R_{BC} = R_{AC} = 1$, beyond which A is heavier than C and C becomes the LSP, which contradicts our original assumption (2.6). For consistency with the earlier notation (N_{jl}, N_{jl}) for the on-shell parameter space regions, we shall simply use $N_{jl} = 4$ to label the single off-shell case for $\{c, d\} = \{(m_{jl(lo)}^{max})^2, (m_{jl(hi)}^{max})^2\}$, and $N_{jll} = 5, 6$ to label the corresponding two off-shell expressions for $b = (m_{jll}^{max})^2$ given in eq. (2.19). This gives us a total of 11 allowed (N_{jl}, N_{jl}) combinations, which are all exhibited in Fig. 2.

2.2 Inversion formulas

Having presented all the “forward” formulas for the five kinematic endpoints a, b, c, d and e in terms of the mass parameters R_{ij} and m_D , we are now in position to tackle the inverse problem: deriving the inverse relations, which would give the mass spectrum m_A, m_B, m_C and m_D in terms of the measured endpoints a, b, c, d and e . Our goal will be to obtain the exact analytical inverse formulas for *each* of the relevant parameter space regions of Fig. 2. Until now, the inverse relations have been derived for only 6 of the 11 regions, namely (1,1), (1,2), (1,3), (4,1), (4,2) and (4,3), and have never included the e measurement [26].

Before we begin, we need to make a decision about the following issue. In general, the system appears to be over-constrained, since we are trying to solve for four unknowns (m_A, m_B, m_C and m_D) in terms of five measurements (a, b, c, d and e). Therefore, for the purpose of inversion, we are allowed to drop one of the five measurements and use only the remaining four. Which measurement should we drop? This question actually turns out to be quite important for the subsequent discussion.

The approach of Ref. [26] (which considered only the on-shell case of Fig. 1(a)) was to eliminate e and use only a, b, c , and d . The reasoning was that the “forward” expression for e (2.15) appears to be too complicated to be tackled by analytic means. However, the problem with this approach is that it cannot be applied in the three on-shell regions (3,1), (3,2) and (2,3), where the three measurements a, b and d are not independent, due to the relation (2.17). Therefore, in order to obtain inverse relations valid over the full parameter space of Fig. 2, *we must make use of the $m_{jll}^{min}(\theta > \frac{\pi}{2})$ measurement* (2.15). For the same reason, we must also use the $m_{jl(lo)}^{max}$ measurement (2.10). Therefore, the choice of candidates to be omitted is narrowed down to three: a, b and d , i.e. precisely the problematic ones entering the linear dependence relation (2.17).

Leaving aside the experimental issues of precision, at this point it should be clear that it is most convenient to drop the b measurement and *always* perform the inversion in terms of a, c, d and e . There are two important advantages of our approach:

- Since we are never using the b measurement, the linear dependence (2.17) between a, b and d never becomes an issue, and the same four inputs a, c, d and e can be used in all parameter space regions (N_{jl}, N_{jll}) .
- More importantly, once we eliminate b from the discussion, we do not have to worry about the division of the parameter space into regions labelled by the integer N_{jll} .

Instead, the full parameter space is now divided just into the four color-coded regions of Fig. 2, each of which is uniquely identified by the value of N_{jl} and from now on will be labelled as $\mathcal{R}_{N_{jl}}$:

1. Region \mathcal{R}_1 ($N_{jl} = 1$), defined by $\frac{1}{2-R_{AB}} < R_{BC} < 1$ and shaded green in Fig. 2.
2. Region \mathcal{R}_2 ($N_{jl} = 2$), defined by $R_{AB} < R_{BC} < \frac{1}{2-R_{AB}}$ and shaded magenta in Fig. 2.
3. Region \mathcal{R}_3 ($N_{jl} = 3$), defined by $0 < R_{BC} < R_{AB}$ and shaded cyan in Fig. 2.
4. Region \mathcal{R}_4 ($N_{jl} = 4$), defined by $1 < R_{BC}$ and shaded yellow in Fig. 2.

In what follows, we sometimes refer to regions \mathcal{R}_1 , \mathcal{R}_2 and \mathcal{R}_3 collectively as the “on-shell” region, and region \mathcal{R}_4 as the “off-shell” region, in reference to whether particle B is on-shell or off-shell. This distinction is in one-to-one correspondence with the distinction between the two-body scenario of Fig. 1(a) and the three-body scenario of Fig. 1(b), respectively. Note that the region identification only depends on the two mass parameters R_{AB} and R_{BC} . For comparison, the original endpoint method utilizing the b measurement, required all eleven regions of Fig. 2, whose definitions depend also on R_{CD} , and one must check the solution for consistency in each region by trial and error [26]. Instead, we have now reduced the number of regions from eleven down to four. Furthermore, in Section 4 we shall show that the shape of the kinematical boundaries of the $m_{jl(hi)}^2$ versus $m_{jl(lo)}^2$ distribution reveal the exact region \mathcal{R}_i in which the mass spectrum occurs, thus eliminating the need for trial-and-error inversion altogether. We consider this to be one of our most important results.

With those preliminaries, we are now ready to present our inversion formulas which can be cast in the following form common to all regions:

$$m_A^2 = G_i (\alpha_i - 1) (\beta_i - 1) (\gamma_i - 1), \quad (2.23)$$

$$m_B^2 = G_i (\alpha_i - 1) (\beta_i - 1) \gamma_i, \quad (2.24)$$

$$m_C^2 = G_i (\alpha_i - 1) \beta_i \gamma_i, \quad (2.25)$$

$$m_D^2 = G_i \alpha_i \beta_i \gamma_i. \quad (2.26)$$

where the subscript $i = 1, 2, 3, 4$ is used to indicate the corresponding (color-coded) region \mathcal{R}_i of Fig. 2. The quantities G_i , α_i , β_i , and γ_i are functions of the measured endpoints $\{a, c, d, e\}$ and are region-dependent, just like the “forward” expressions for the endpoints in terms of the input masses (see Sec. 2.1). Before defining G_i , α_i , β_i , and γ_i , we identify an ubiquitous combination of observables

$$g \equiv 2e - a \quad (2.27)$$

and use it in place of e , so that our starting point is the equivalent set of four measurements $\{a, c, d, g\}$. Then the quantities appearing on the right hand side of eqs. (2.23-2.26) are

defined by

$$G_1 \equiv \frac{g(2d-g) - 2c(d-g)}{g}, \quad \alpha_1 \equiv \frac{a+G_1}{G_1}, \quad \beta_1 \equiv \frac{d}{G_1}, \quad \gamma_1 \equiv \frac{c}{G_1}; \quad (2.28)$$

$$G_2 \equiv \frac{g(2d-g)(d-c)}{g(d-c) + 2c(d-g)}, \quad \alpha_2 \equiv \frac{a+G_2}{G_2}, \quad \beta_2 \equiv \frac{d}{G_2}, \quad \gamma_2 \equiv \frac{c}{d-c}; \quad (2.29)$$

$$G_3 \equiv \frac{(g(2d-g) - 2c(d-g))d}{gd + 2c(d-g)}, \quad \alpha_3 \equiv \frac{a+G_3}{G_3}, \quad \beta_3 \equiv \frac{c(d+G_3)}{dG_3}, \quad \gamma_3 \equiv \frac{d}{G_3}; \quad (2.30)$$

$$G_4 = -d + g + \sqrt{(2d-g)g}, \quad \alpha_4 = \frac{a+G_4}{G_4}, \quad \beta_4 = \gamma_4 = \frac{d+G_4}{2G_4}. \quad (2.31)$$

A word of caution is in order regarding the off-shell scenario of Fig. 1(b), i.e. eq. (2.31). In that case, particle B is far off-shell and its mass m_B is not among the relevant parameters for the kinematic endpoints⁹, so that we only need to determine three unknowns: m_A , m_C and m_D . At the same time, we have one fewer independent inputs within our original set $\{a, c, d, g\}$, since eqs. (2.20) and (2.21) imply the additional relation

$$c = \frac{1}{2}d. \quad (2.32)$$

For the purpose of inversion, in the off-shell case we chose to omit c and work only with $\{a, d, g\}$, which are the only three endpoints appearing in eq. (2.31). Finally, the appearance of the square root in (2.31) should not be a problem, since in the off-shell scenario the ratio $\frac{d}{g}$ is bounded by

$$1 < \frac{d}{g} < 2 + \sqrt{2}. \quad (2.33)$$

The set of analytical inversion formulas (2.23-2.26,2.28-2.31) is the first main result of this paper.

3. Duplication analysis

Armed with the analytical results from the previous section, we are now ready to address the problem of duplicate solutions and the potential discrete ambiguities in the determination of the mass spectrum. Our procedure will be very simple and straightforward. We shall consider the four (color-coded) parameter space regions \mathcal{R}_i in Fig. 2 one at a time, and in each case we shall ask the question: Is it possible that identically the same values of the endpoints $\{a, c, d, e\}$ can be obtained from another type of mass spectrum belonging to a *different* parameter space region \mathcal{R}_j , with $j \neq i$? And if the answer is “yes”, we shall then ask two follow-up questions: First, exactly in which parts of \mathcal{R}_i and \mathcal{R}_j does this duplication occur? Second, will the ambiguity get resolved by utilizing the additional endpoint measurement b at our disposal?

⁹Of course, (2.24) should only be used in the on-shell case.

Operationally we proceed as follows. First, it is important to realize that the “forward” analytical formulas of Section 2.1 provide a map \mathcal{F}_i of the corresponding parameter space region \mathcal{R}_i onto the space of values of the kinematic endpoints:

$$\{m_A, m_B, m_C, m_D\}_i \xrightarrow{\mathcal{F}_i} \{a, c, d, e\}, \quad (3.1)$$

or equivalently, using the reparametrization (2.7)

$$\{m_D, R_{AB}, R_{BC}, R_{CD}\}_i \xrightarrow{\mathcal{F}_i} \{a, c, d, e\}. \quad (3.2)$$

Similarly, the inverse formulas from Section 2.2 provide an inverse map \mathcal{F}_i^{-1} from the space of kinematical endpoints back onto the mass parameter space:

$$\{a, c, d, e\} \xrightarrow{\mathcal{F}_j^{-1}} \{m_D, R_{AB}, R_{BC}, R_{CD}\}_j. \quad (3.3)$$

The composite of the two maps (3.2) and (3.3) for $i \neq j$, is a transformation

$$T_{ij} \equiv \mathcal{F}_j^{-1} \cdot \mathcal{F}_i \quad (3.4)$$

relating parameter space points belonging to two *different* regions, \mathcal{R}_i and \mathcal{R}_j , yet resulting in *identical* kinematical endpoints $\{a, c, d, e\}$:

$$\{m_D, R_{AB}, R_{BC}, R_{CD}\}_i \xrightarrow{T_{ij}} \{m'_D, R'_{AB}, R'_{BC}, R'_{CD}\}_j. \quad (3.5)$$

The transformation T_{ij} described in (3.5) will serve as the basis of our duplication analysis. The exact analytical formulas for this mapping can be trivially obtained from our analytical results above in Section 2, but are rather lengthy and we shall not present them here explicitly. However, we note that in the three on-shell cases $i = 1, 2, 3$ they have the generic form

$$R'_{AB} = f_{AB}(R_{AB}, R_{BC}), \quad (3.6)$$

$$R'_{BC} = f_{BC}(R_{AB}, R_{BC}), \quad (3.7)$$

$$R'_{CD} = f_{CD}(R_{AB}, R_{BC}, R_{CD}), \quad (3.8)$$

$$m'_D = m_D f_D(R_{AB}, R_{BC}, R_{CD}), \quad (3.9)$$

where f_{AB} , f_{BC} , f_{CD} and f_D are the functions defining the transformation T_{ij} . One important feature of the T_{ij} map (3.6-3.9) is that it transforms the 2-dimensional subspace of dimensionless parameters $\{R_{AB}, R_{BC}\}$ into itself. Notice that R_{AB} and R_{BC} are precisely the parameters defining the four regions \mathcal{R}_i in Fig. 2. Therefore, for the purposes of our duplication analysis it is sufficient to consider the simpler transformation of

$$\{R_{AB}, R_{BC}\}_i \xrightarrow{T_{ij}} \{R'_{AB}, R'_{BC}\}_j \quad (3.10)$$

given by eqs. (3.6) and (3.7) only, instead of the more general mapping (3.5) given by all four eqs. (3.6-3.9).

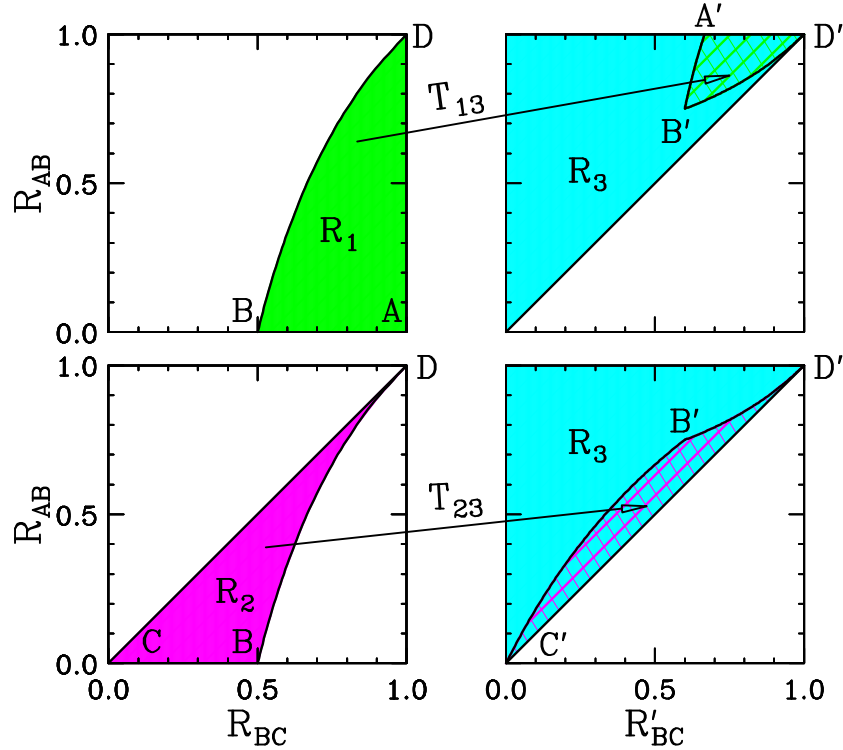


Figure 3: The maps $T_{13} : \mathcal{R}_1 \mapsto \mathcal{R}_3$ (top two panels) and $T_{23} : \mathcal{R}_2 \mapsto \mathcal{R}_3$ (bottom two panels), which are implied by eq. (3.10). In both cases the target region \mathcal{R}_3 is shaded in cyan. Under T_{13} , the green-shaded region ABD in the top left panel transforms into the green-hatched region $A'B'D'$ of the top right panel. Under T_{23} , the magenta-shaded region BCD in the bottom left panel transforms into the magenta-hatched region $B'C'D'$ of the bottom right panel. In both cases, the transformed (primed) region falls completely within the boundaries of the intended target (\mathcal{R}_3).

We are now ready to answer the main question posed at the beginning of this section: does a consistent mapping (3.10) exist for *some* pair of regions \mathcal{R}_i and \mathcal{R}_j ? Note that the transformation (3.10) is not necessarily always well defined: consistency requires that the obtained values of $\{R'_{AB}, R'_{BC}\}_j$ belong to Region \mathcal{R}_j , which is not automatically guaranteed and must be explicitly checked. To put this in more formal terms, we are only interested in those cases where the intersection of the image of region \mathcal{R}_i under the transformation T_{ij} and the intended target region \mathcal{R}_j is a non-empty set:

$$\{T_{ij}(\mathcal{R}_i)\} \cap \{\mathcal{R}_j\} \neq \emptyset. \quad (3.11)$$

In order to find all such occurrences, we consider all possible transformations T_{ij} with $i \neq j$ and enforce the consistency check (3.11).

We begin with the on-shell case ($i, j = 1, 2, 3$), where there are 6 possible mappings T_{ij} . For the purposes of finding the duplicated portion of parameter space, it is sufficient to consider only 3 of them, which for convenience of illustration we choose as T_{13} , T_{23} and T_{21} . The corresponding results are shown in Figs. 3 and 4. Fig. 3 shows the effect of the transformation $T_{13} : \mathcal{R}_1 \mapsto \mathcal{R}_3$ (top two panels) and $T_{23} : \mathcal{R}_2 \mapsto \mathcal{R}_3$ (bottom two panels),

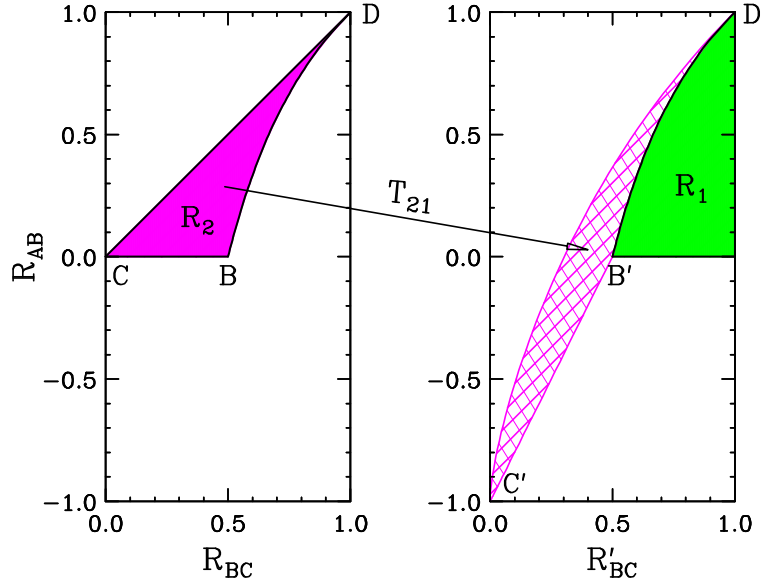


Figure 4: The same as Fig. 3, but for the map $T_{21} : \mathcal{R}_2 \mapsto \mathcal{R}_1$, where the intended target is the green-shaded region \mathcal{R}_1 . Under T_{21} , the magenta-shaded region BCD in the left panel transforms into the magenta-hatched region $B'C'D'$ of the right panel. The image $B'C'D'$ has no overlap with its intended target \mathcal{R}_1 , except along the $BD = B'D'$ boundary, which is left invariant under the T_{12} transformation.

while Fig. 4 shows the map $T_{21} : \mathcal{R}_2 \mapsto \mathcal{R}_1$. In both figures, the color-shaded areas in the left (right) panels exhibit the original regions \mathcal{R}_i (the intended target regions R_j). The cross-hatched areas in the right panels depict the actual image $T_{ij}(\mathcal{R}_i)$ of the \mathcal{R}_i region under the transformation T_{ij} . For example, in Fig. 3 T_{13} maps the whole green-shaded region ABD on the left into the green-hatched region $A'B'D'$ on the right, while in Fig. 3 (Fig. 4) T_{23} (T_{21}) maps the whole magenta-shaded region BCD on the left into the magenta-hatched region $B'C'D'$ on the right. In accordance with (3.11), duplication occurs whenever the right panels in Figs. 3 and 4 exhibit an overlap between the cross-hatched area of the image and the solid color-shaded area of the intended target. We see that duplication occurs in the case of T_{13} and T_{23} , but not for T_{21} , although in the latter case points which are on opposite sides, but close to the boundary line BD will give rather similar values for the measured kinematic endpoints $\{a, c, d, e\}$.

At this point one may wonder whether the result of Fig. 3 is sufficient to prove the existence of duplication. Indeed, Fig. 3 tells us nothing about the remaining two parameters R_{CD} and m_D and more specifically about their transformed values R'_{CD} and m'_D under the mappings T_{13} and T_{23} . Duplication will in fact not occur, if R'_{CD} and m'_D turn out to be unphysical, for example, if $R'_{CD} < 0$, $R'_{CD} > 1$ or $(m'_D)^2 < 0$. Unfortunately, a closer inspection of (3.8) reveals that

$$f_{CD}(R_{AB}, R_{BC}, R_{CD} = 0) = 0, \quad (3.12)$$

$$f_{CD}(R_{AB}, R_{BC}, R_{CD} = 1) = 1, \quad (3.13)$$

for any values of R_{AB} and R_{BC} , so that R_{CD} is always consistently mapped within its definition region. Similarly, we find no problem with eq. (3.9). Therefore, the duplication examples shown in Fig. 3 truly represent a problem.

We then perform a similar analysis involving the off-shell region \mathcal{R}_4 and find no occurrences of duplication, which is not surprising, since the off-shell case is more restricted, due to (2.32). Therefore, Figs. 3 and 4 already provide the final answer to the first question posed at the beginning of this Section: which portions of the mass parameter space (2.7) exhibit exact duplication? We can summarize our result as follows:

For every point with $R_{AB} < R_{BC} < 1$ (i.e. in region \mathcal{R}_1 or \mathcal{R}_2) and arbitrary values of R_{CD} and m_D , there exists another parameter space point with $R_{BC} < R_{AB} < 1$ and certain (in general different) values of R_{CD} and m_D , which would result in *identical* predictions for all four kinematic endpoints $\{a, c, d, e\}$.

The reverse statement is not true: not every point with $R_{BC} < R_{AB} < 1$ (i.e. in region \mathcal{R}_3) is subject to duplication. Referring to the right panels of Fig. 3, only the cross-hatched portions of the cyan-shaded region \mathcal{R}_3 are duplicated.

Having found duplication examples for the limited set of measurements $\{a, c, d, e\}$, it is now time to ask whether the additional measurement of the b kinematic endpoint will help. We find that, as might have been expected, whenever the b measurement is independent of the others, the duplication goes away. Unfortunately, as already mentioned in the discussion following eq. (2.17), in the three subregions (3,1), (3,2) and (2,3), b is not an independent measurement, and thus the duplication will persist even for the full set of 5 measurements $\{a, b, c, d, e\}$! In terms of the subregions of Fig. 2, the two cases of duplication found in Fig. 3 can then be summarized as

$$(3, 1) \xrightarrow{T_{13}} (2, 3), \quad (3.14)$$

$$(3, 2) \xrightarrow{T_{23}} (2, 3). \quad (3.15)$$

As long as the original parameter space point and its image belong to these particular subregions, the resulting two sets of endpoints (1.7) will be identical.

We caution the reader not to get the impression from (3.14) and (3.15) that *every* parameter space point in regions (3,1), (3,2) and (2,3) is duplicated with something. Recall that the boundaries of the dangerous subregions (3,1), (3,2) and (2,3) depend on R_{CD} , thus the range of R_{CD} values resulting in duplication will now be restricted. Therefore, in the presence of the additional b measurement, our previous statement about duplication is now modified as follows:

For every point with $R_{AB} < R_{BC} < 1$ and *any* m_D , there exists a range of R_{CD} for which exactly the same values of the five kinematic endpoint measurements $\{a, b, c, d, e\}$ can also be obtained from a different parameter space point with $R_{BC} < R_{AB} < 1$ and some other (generally different) values of R_{CD} and m_D .

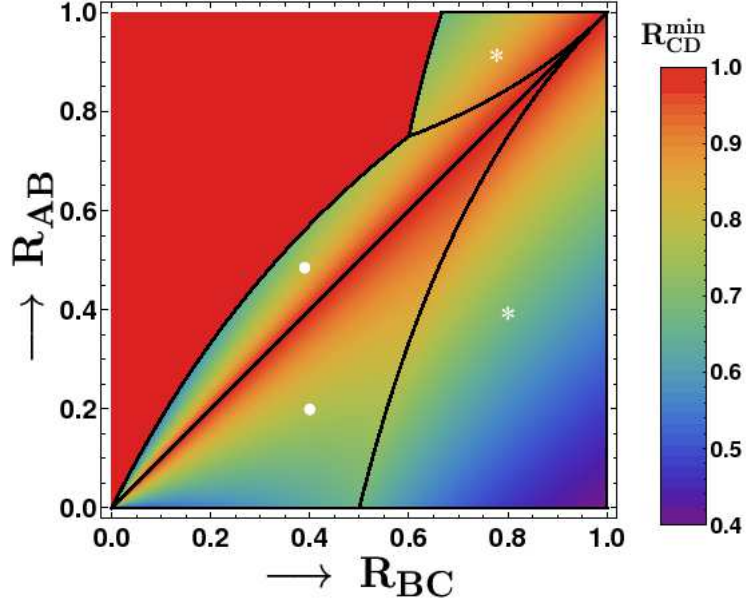


Figure 5: The minimum value $R_{CD}^{\min}(R_{BC}, R_{AB})$ required for duplication, as a function of R_{BC} and R_{AB} . The white asterisks (circles) mark the duplicate pair of points P_{31} and P_{23} (P_{32} and P'_{23}) in Table 2.

We shall now describe the duplicated parameter space implied by (3.14) and (3.15) a bit more quantitatively. As we just mentioned, for any given point in the (R_{BC}, R_{AB}) plane, there may exist a range of values for R_{CD} which would cause duplication. Let us denote the minimum and maximum values of that range by R_{CD}^{\min} and R_{CD}^{\max} , correspondingly. Clearly, both R_{CD}^{\min} and R_{CD}^{\max} are in general functions of R_{BC} and R_{AB} . Then, the “duplicated” parameter space can be simply described as the set of all points $\{R_{AB}, R_{BC}, R_{CD}\}$, which satisfy the two inequalities

$$R_{CD}^{\min}(R_{BC}, R_{AB}) < R_{CD} < R_{CD}^{\max}(R_{BC}, R_{AB}). \quad (3.16)$$

If, on the other hand, the values of R_{BC} and R_{AB} are such that duplication does not occur for *any* value of R_{CD} , we can simply take $R_{CD}^{\min} = R_{CD}^{\max}$, resulting in a set of zero measure for (3.16).

Now, in order to delineate the duplicated parameter space, we only need to supply its boundaries $R_{CD}^{\min}(R_{BC}, R_{AB})$ and $R_{CD}^{\max}(R_{BC}, R_{AB})$. Our analysis reveals that within the duplication region we always find

$$R_{CD}^{\max}(R_{BC}, R_{AB}) = 1, \quad (3.17)$$

while the function $R_{CD}^{\min}(R_{BC}, R_{AB})$ is plotted in Fig. 5. Duplication does not occur in the uniformly red region in the upper left corner, so there we choose to plot $R_{CD}^{\min} = R_{CD}^{\max} = 1$, in accordance with our convention. Within the rainbow-colored region in Fig. 5, duplication will exist for any value of R_{CD} , as long as R_{CD} is larger than the R_{CD}^{\min} value shown in the

figure, i.e. for

$$R_{CD}^{\min}(R_{BC}, R_{AB}) < R_{CD} < 1, \quad (3.18)$$

where we have made use of (3.17). Fig. 5 reveals that the duplication region is typically characterized by a rather high¹⁰ value of $R_{CD} = m_C^2/m_D^2$. This implies that in order to have duplication, particle D cannot be too much heavier than particle C . This situation does not often arise in typical SUSY models, where D is a squark \tilde{q} and C is the second-lightest (wino-like) neutralino $\tilde{\chi}_2^0$. In models with a high SUSY breaking scale like SUGRA, the Renormalization Group Equation (RGE) running tends to split the squark and electroweak gaugino masses, so that the hierarchy $m_D \sim m_C$ is rather unlikely. On the other hand, minimal UED models predict a rather degenerate spectrum, since the mass splittings arise mostly at the loop level, so that $m_D \sim m_C$ is rather natural in this case [8].

As an illustration of the whole duplication discussion so far, let us now choose two specific examples of duplicate mass spectra, one for the case of (3.14) and another for the case of (3.15). The corresponding input masses and mass ratios, as well as the resulting kinematic endpoints, are shown in Table 2. The first five kinematic endpoints shown in the Table were already discussed, while the rest are new and will be introduced below in Sections 4 and 5. As an application of our previous results, let us outline our procedure of selecting each pair of study points in Table 2. Let us start with the case of (3.14). Since we know from Fig. 5 that the whole region (3,1) is duplicated, it is convenient to first choose the point from that region. We select nice round numbers like $R_{AB} = 0.4$ and $R_{BC} = 0.8$. This choice is indicated in Fig. 5 with the white asterisk inside region \mathcal{R}_1 . Then Fig. 5 shows that $R_{CD}^{\min} = 0.686$, therefore we choose a somewhat larger value: $R_{CD} = 0.7$. This choice of R_{AB} , R_{BC} and R_{CD} already guarantees duplication for any value of m_D , and we choose $m_D = 500$ GeV (another nice round number). The resulting masses m_A , m_B and m_C can be readily computed in terms of m_D and the mass ratios. We call the resulting spectrum “study point P_{31} ”, which is listed in the second column of Table 2. Given P_{31} , one can use the transformation T_{13} to obtain the matching spectrum in region (2,3), which is listed in the third column of Table 2 under the name of “study point P_{23} ”. In the case of (3.15), we follow a similar procedure, except we start with a point in region \mathcal{R}_2 (indicated with a white circle in Fig. 5) and then use the T_{23} transformation to obtain the corresponding point in region (2,3). The two resulting mass spectra (called P_{32} and P'_{23}) are given in the fourth and fifth column of Table 2, respectively.

In the on-shell case the parameters $\{R_{AB}, R_{BC}, R_{CD}\}$ belong to a unit cube, due to the restrictions (2.5). The volume of the unit cube is 1. Fig. 5 then allows us to calculate the volume fraction of this unit cube which corresponds to a duplicated parameter space region. The result that we find is 0.158. Then one might be tempted to say that if new physics like supersymmetry or UED with a cascade decay of the type shown in Fig. 1(a) is discovered at the LHC, there would be roughly a 15.8% probability that endpoint measurements alone would result in a duplicate spectrum, even under ideal experimental conditions. However, it is rather difficult to justify such probabilistic statements, since they are not invariant under

¹⁰The minimum value of R_{CD} that we find over the whole parameter region in Fig. 5 is $R_{CD} = 0.4$ and is found at $R_{BC} = 1$, $R_{AB} = 0$.

Variable	$\mathcal{R}_1 \leftrightarrow \mathcal{R}_3$		$\mathcal{R}_2 \leftrightarrow \mathcal{R}_3$	
	(3,1)	(2,3)	(3,2)	(2,3)
	P_{31}	P_{23}	P_{32}	P'_{23}
m_A (GeV)	236.643	915.618	126.491	241.618
m_B (GeV)	374.166	954.747	282.843	346.073
m_C (GeV)	418.33	1083.10	447.214	554.133
m_D (GeV)	500.00	1172.57	500.00	610.443
R_{AB}	0.400	0.920	0.200	0.487
R_{BC}	0.800	0.777	0.400	0.390
R_{CD}	0.700	0.853	0.800	0.824
R_{CD}^{min}	0.686	0.845	0.774	0.800
m_{ll}^{max} (GeV)	\sqrt{a}	145		310
m_{jll}^{max} (GeV)	\sqrt{b}	257		369
$m_{jl(lo)}^{max}$ (GeV)	\sqrt{c}	122		149
$m_{jl(hi)}^{max}$ (GeV)	\sqrt{d}	212		200
$m_{jll(\theta>\frac{\pi}{2})}^{min}$ (GeV)	\sqrt{e}	132		248
$m_{jl_f}^{max}$ (GeV)	\sqrt{f}	212	127	200
$m_{jl_f}^{(p)}$ (GeV)	\sqrt{p}	190	112	126
$m_{jl_n}^{max}$ (GeV)	\sqrt{n}	122	212	173
$m_{jl(eq)}^{max}$ (GeV)	\sqrt{q}	NA	122	149
$m_{jll(+)}(0)$ (GeV)	\sqrt{s}	226	240	214
$m_{jll(+)}(a_t)$ (GeV)	\sqrt{t}	263	257	374
$m_{jll(+)}(a_{on})$ (GeV)	\sqrt{u}	257	257	369
$m_{jll(-)}(a_{on})$ (GeV)	\sqrt{v}	190	193	355
$m_{jll(+)}(a_{off})$ (GeV)	\sqrt{w}	256	243	372
				367

Table 2: Two examples of *exact* duplication as implied by (3.14) and (3.15). The pairs of study points P_{31} and P_{23} , as well as P_{32} and P'_{23} , exhibit identical values for all five kinematic endpoints m_{ll}^{max} , m_{jll}^{max} , $m_{jl(lo)}^{max}$, $m_{jl(hi)}^{max}$ and $m_{jll(\theta>\frac{\pi}{2})}^{min}$. Point P_{31} belongs to Region \mathcal{R}_1 , point P_{32} belongs to Region \mathcal{R}_2 , while points P_{23} and P'_{23} belong to Region \mathcal{R}_3 . In Fig. 5, the duplicate pair of points P_{31} and P_{23} (P_{32} and P'_{23}) is marked with white asterisks (white circles). The second-to-last and last blocks in the table contain the endpoint measurements which are available from the two-dimensional distributions $(m_{jl(lo)}^2, m_{jl(hi)}^2)$ and (m_{ll}^2, m_{jll}^2) , discussed below in Sections 4 and 5, correspondingly.

reparametrizations, and furthermore, they depend on the assumed (usually uniform) prior for the probability distribution of new physics models in mass parameter space. Any given model of SUSY breaking, for example, would select a preferred parameter space within the unit cube, and may lower or increase this naively calculated probability. The generic mass degeneracy in UED, on the other hand, would prefer the region $R_{AB} \sim R_{BC} \sim R_{CD} \sim 1$,

and the duplication is much more likely. The important result from our point of view is that there *exists* a non-vanishing duplication region, and this fact alone is sufficient to motivate us to look for alternative methods for mass determination, which we shall undertake in the following two sections.

4. Kinematic boundary lines for the $m_{jl(lo)}^2$ versus $m_{jl(hi)}^2$ distribution

In this section we shall analyze the shape of the *two-dimensional* invariant mass distribution

$$\frac{d^2\Gamma}{dm_{jl(lo)}^2 dm_{jl(hi)}^2}, \quad (4.1)$$

which we imagine plotted as either a scatter plot or a two-dimensional histogram with $m_{jl(lo)}^2$ on one axis and $m_{jl(hi)}^2$ on the other¹¹. The purpose of our analysis will be twofold. On the one hand, we shall be interested whether we can use the shape of this two-dimensional distribution to resolve the mass spectrum duplication problem encountered in the previous section. But more importantly, we shall investigate what *additional* kinematic endpoint measurements besides those already considered in (1.7), may become available in this case.

Recall that the variables $m_{jl(lo)}$ and $m_{jl(hi)}$ were introduced in eqs. (1.1) and (1.2) as a way to deal with the ambiguity in the experimental identification of the “near” and “far” leptons l_n^\pm and l_f^\mp in Fig. 1. It is therefore not very surprising that the shape of the $m_{jl(lo)}$ versus $m_{jl(hi)}$ distribution (4.1) that we are interested in, is very closely related to the corresponding $m_{jl_n}^2$ versus $m_{jl_f}^2$ distribution

$$\frac{d^2\Gamma}{dm_{jl_n}^2 dm_{jl_f}^2}. \quad (4.2)$$

In principle, both distributions (4.1) and (4.2) depend not only on the mass spectrum, but also on the spins and on the chiralities of the coupling constants of the particles A, B, C and D involved in the cascade [67, 68, 80]. However, the location and the shape of the boundary lines in the scatter plots (4.1) and (4.2) are determined purely by kinematics, and do not depend on the spin and type of couplings. To the extent that we are only interested in these boundary lines, it is therefore sufficient to ignore spin effects and consider only pure phase space decays, in which case the analytical results for the distributions (4.2) and (4.1) are in principle already available [30]. From now on, the term “shape” will therefore refer to the location and shape of the boundary lines, and will otherwise have nothing to do with the probability density of the two-dimensional distributions such as (4.1) or (4.2).

In the on-shell case, the shape of the $m_{jl_n}^2$ versus $m_{jl_f}^2$ invariant mass distribution (4.2) is extremely simple, and is illustrated in Fig. 6. The scatter plot in the $(m_{jl_n}^2, m_{jl_f}^2)$ plane fills the right-angle trapezoid $ONPF$, whose corner points are defined as follows. Point O is

¹¹In practice, as we shall demonstrate below, it may be more convenient to plot the *linear* masses $m_{jl(lo)}$ and $m_{jl(hi)}$ on the two axes, but use a quadratic power scale instead of the conventional linear or logarithmic scales.

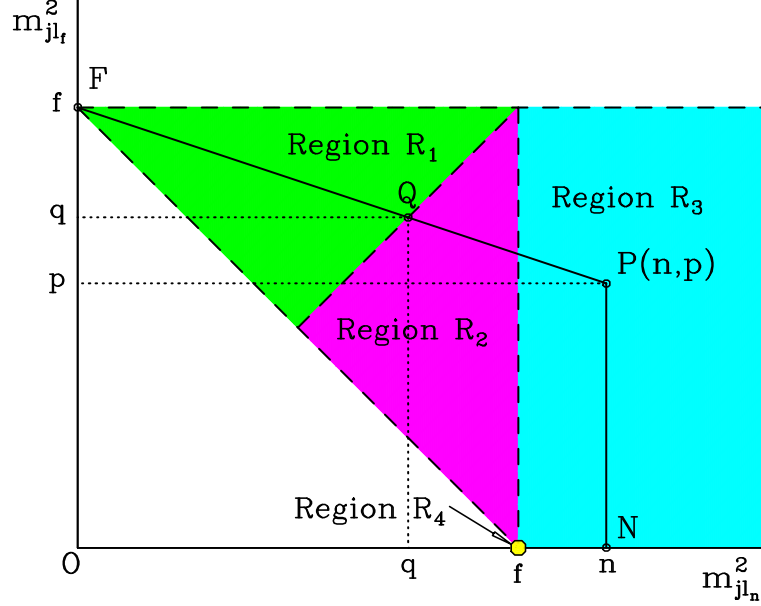


Figure 6: The generic shape $ONPF$ of the bivariate distribution (4.2) in the $(m_{jl_n}^2, m_{jl_f}^2)$ plane.

simply the origin of the coordinate system. Point N (for “near”) lies on the $m_{jl_n}^2$ axis, and its coordinate is nothing but the maximum possible value of the jet-near lepton invariant mass

$$n \equiv (m_{jl_n}^{max})^2 = m_D^2 (1 - R_{CD}) (1 - R_{BC}), \quad (4.3)$$

which was already introduced in eq. (2.12). Similarly, point F (for “far”) lies on the $m_{jl_f}^2$ axis, and its coordinate is nothing but the maximum possible value of the jet-far lepton invariant mass

$$f \equiv (m_{jl_f}^{max})^2 = m_D^2 (1 - R_{CD}) (1 - R_{AB}), \quad (4.4)$$

which was already defined in eq. (2.13). Finally, the point P is the most important of the four corners, since it defines the actual shape of the trapezoid, once points N and F are fixed. The coordinates of point P in the $(m_{jl_n}^2, m_{jl_f}^2)$ plane are (n, p) , where n was already defined in (4.3), while p is a *new* quantity:

$$p \equiv (m_{jl_f}^{(p)})^2 \equiv f R_{BC} = m_D^2 (1 - R_{CD}) R_{BC} (1 - R_{AB}). \quad (4.5)$$

Since N and P share the same $m_{jl_n}^2$ coordinate n , point P always lies directly above point N . At the same time, the definition of p implies that

$$p < f, \quad (4.6)$$

so that point P always lies lower than point F , as illustrated in Fig. 6. Finally, in Regions \mathcal{R}_2 and \mathcal{R}_3 , there is one more special point, Q , which can be seen in Fig. 6: it is the point where the FP side of the trapezoid intersects the 45° line $m_{jl_n}^2 = m_{jl_f}^2$. The two coordinates

of point Q are equal by definition, and are given by

$$q \equiv \left(m_{jl(eq)}^{max} \right)^2 = m_D^2 (1 - R_{CD}) \frac{1 - R_{AB}}{2 - R_{AB}}, \quad (4.7)$$

which is nothing but the quantity previously defined in eq. (2.14). The four quantities n , p , f and q just introduced are not all independent, but obey the relation

$$\frac{f}{q} = 1 + \frac{f - p}{n}. \quad (4.8)$$

With those conventions, the trapezoid $ONPF$ can be equivalently defined through the parametric equation of the boundary line segment FP . A convenient choice for the line parameter is the running value of $m_{jl_n}^2$. Then the parametric equation of the line FP is given by

$$FP : \quad m_{jl_f}^2 (m_{jl_n}^2) = f - \frac{f - p}{n} m_{jl_n}^2. \quad (4.9)$$

In terms of this parametrization, the three special $m_{jl_f}^2$ values introduced in Fig. 6 are given as follows:

$$f = m_{jl_f}^2(0), \quad (4.10)$$

$$p = m_{jl_f}^2(n), \quad (4.11)$$

$$q = m_{jl_f}^2(q). \quad (4.12)$$

The last equation is exactly the relation (4.8).

The color-coded regions in Fig. 6 show the allowed locations of point P , and are in one-to-one correspondence with the color-coded parameter space regions of Fig. 2 (in both cases we use the same color coding). This correspondence is most easily seen as follows. First, note that the two white areas in Fig. 6 are not accessible to point P . The region with $m_{jl_f}^2 > f$ is forbidden due to the relation (4.6). Similarly, the white triangular area near the origin, defined by

$$m_{jl_f}^2 < f - m_{jl_n}^2 \quad (4.13)$$

is also not allowed, which can be seen by using the inequality

$$p \geq f - n, \quad (4.14)$$

following from the defining relations (4.3-4.5). Therefore, point P must belong to one of the three colored regions in Fig. 6. As can be seen from the figure, these three regions are distinguished based on the value of n relative to f and p : recall that eq. (4.6) already determines the hierarchy $p < f$, so that for n there are only three possible options: n can be smaller than p , n can be larger than f , or n can fall in between p and f . Let us consider each case in turn.

1. The case $n < p < f$. Point P then lies somewhere within the green-shaded area in Fig. 6. Using (4.3-4.5), it is easy to see that the conditions $n < p < f$ imply

$$n < p < f \implies \frac{1}{2 - R_{AB}} < R_{BC} < 1, \quad (4.15)$$

which was precisely the defining relation for region \mathcal{R}_1 in Fig. 2. Therefore, in Fig. 6 we have labelled and color-coded the area with $n < p < f$ to match the notation for region \mathcal{R}_1 used in Fig. 2.

2. The case $p < n < f$. In this case point P would belong to the magenta-shaded triangular area in Fig. 6. The conditions $p < n < f$ now imply

$$p < n < f \implies R_{AB} < R_{BC} < \frac{1}{2 - R_{AB}}, \quad (4.16)$$

which is the definition of region \mathcal{R}_2 in Fig. 2. Once again, we label and color-code this region to match the notation used in Fig. 2.

3. The case $p < f < n$. Now the point P should fall somewhere within the cyan-shaded semi-infinite rectangular strip in Fig. 6. Using (4.3-4.5), the constraints $p < f < n$ now translate into

$$p < f < n \implies 0 < R_{BC} < R_{AB}, \quad (4.17)$$

which is the definition of region \mathcal{R}_3 in Fig. 2, again justifying the notation and color-coding used in Fig. 6.

Unlike the three on-shell cases just discussed, the off-shell scenario of Fig. 1(b) should be handled with care, since the ‘‘near’’ and ‘‘far’’ lepton distinctions become meaningless in that case. Nevertheless, the off-shell scenario can still be represented in Fig. 6, and in fact this representation is unique: there is a single allowed location for point P at $n = f$ and $p = 0$. In Fig. 6 this unique location is indicated with a yellow-shaded circle, which corresponds to the whole yellow-shaded region \mathcal{R}_4 in Fig. 2. In other words, in the off-shell case we can randomly assign ‘‘near’’ and ‘‘far’’ labels to the two leptons in each event, and then the shape ONF of the resulting $(m_{jl_n}^2, m_{jl_f}^2)$ scatter plot will be an isosceles right triangle.

From the preceding discussion it should be clear that the two-dimensional theoretical distribution (4.2) contains a great deal of useful information: its shape uniquely identifies the on-shell parameter space region \mathcal{R}_i , and yields the four measurements $\{n, f, p, q\}$ given in eqs. (4.3-4.5) and (4.7) instead of the usual two $(m_{jl(lo)}^{\max}, m_{jl(hi)}^{\max})$. Ideally, one would like to preserve and subsequently extract this additional information from the experimentally observable two-dimensional distribution (4.1) as well. We shall now show that this is in fact possible, using the simple intuitive understanding of the shape exhibited in Fig. 6.

The key is to realize that the reordering (1.1) and (1.2) of the $(m_{jl_n}^2, m_{jl_f}^2)$ pair into a $(m_{jl(lo)}^2, m_{jl(hi)}^2)$ pair in geometrical terms simply corresponds to ‘‘folding’’ the trapezoid $ONPF$ in Fig. 6 along the 45° line $m_{jl_n}^2 = m_{jl_f}^2$. This procedure is shown pictorially in Fig. 7, where for illustration we use an example from region \mathcal{R}_3 , i.e. $p < f < n$. Panel

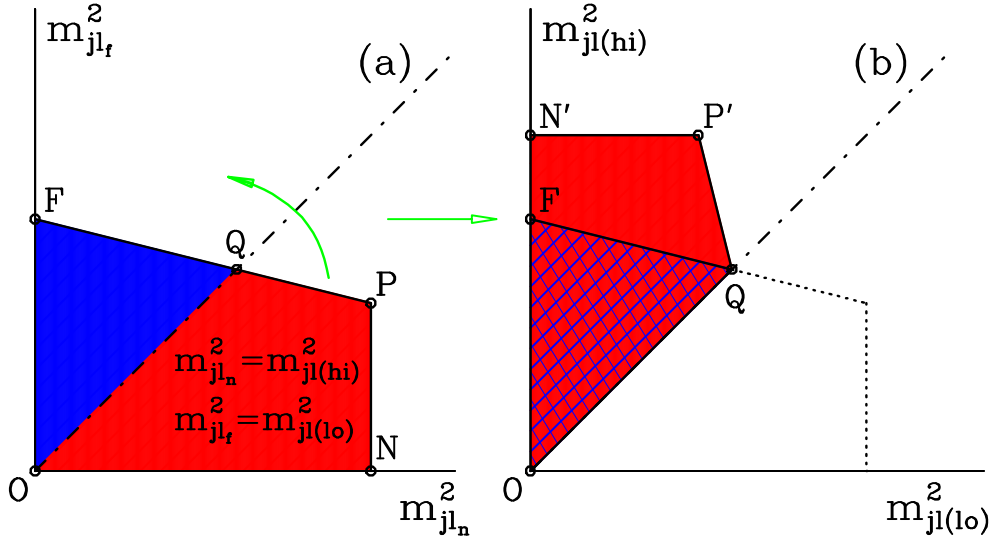


Figure 7: Obtaining the shape of the $m_{jl(lo)}^2$ versus $m_{jl(hi)}^2$ bivariate distribution by folding the $m_{jl_n}^2$ versus $m_{jl_f}^2$ distribution across the line $m_{jl_n}^2 = m_{jl_f}^2$. This particular example applies to region \mathcal{R}_3 . For the other three regions, refer to Figs. 8(a), 8(b) and 8(d).

(a) shows the trapezoidal shape of the original $m_{jl_n}^2$ versus $m_{jl_f}^2$ invariant mass distribution from Fig. 6. Now suppose that we want to convert this $(m_{jl_n}^2, m_{jl_f}^2)$ scatter plot into a $(m_{jl(lo)}^2, m_{jl(hi)}^2)$ scatter plot, simply by reinterpreting the $m_{jl_n}^2$ axis as $m_{jl(lo)}^2$ and the $m_{jl_f}^2$ axis as $m_{jl(hi)}^2$. From that point of view, the trapezoid $ONPF$ in Fig. 7 divides into two adjacent regions: OQF (blue-shaded) and $ONPQ$ (red-shaded). Within the blue-shaded area OQF we have $m_{jl_n}^2 < m_{jl_f}^2$, so that the coordinate pair $(m_{jl_n}^2, m_{jl_f}^2)$ can be directly identified with $(m_{jl(lo)}^2, m_{jl(hi)}^2)$. Thus the blue-shaded area OQF in panel (a) remains unchanged and appears identically in panel (b), where it is marked with a blue cross-hatch. In contrast, within the red-shaded area $ONPQ$ of panel (a), the coordinates $m_{jl_n}^2$ and $m_{jl_f}^2$ are in the wrong order, and need to be reversed when going to the $(m_{jl(lo)}^2, m_{jl(hi)}^2)$ scatter plot of panel (b). In layman terms, this reversal corresponds to “folding” the trapezoid $ONPF$ along the 45° line OQ , as shown in Fig. 7. The resulting image $ON'P'Q$ in Fig. 7(b) is then overlaid on the original region OQF . We see that any $(m_{jl(lo)}^2, m_{jl(hi)}^2)$ scatter plot will therefore exhibit two characteristic types of population density. For example, in the *blue-hatched* red area of Fig. 7(b) we expect the density of points to roughly double, since the folded distribution $ON'P'Q$ is overlaid on top of the existing distribution OQF underneath. In Fig. 8 below, we shall mark such “double-density” regions with a blue cross-hatch in addition to the solid red shading. In contrast, region $FQP'N'$ in Fig. 7(b) is a “single density” region, since the folded distribution happened to fall onto empty space, where originally there were no points to begin with. A single density region can also be obtained when portions of the original $(m_{jl_n}^2, m_{jl_f}^2)$ scatter plot are not overlaid in the process of folding. In either case, we shall denote a single-density region by a solid (red) color-shading, but no cross-hatch.

We are now ready to apply the intuition gained from Figs. 6 and 7 and identify the

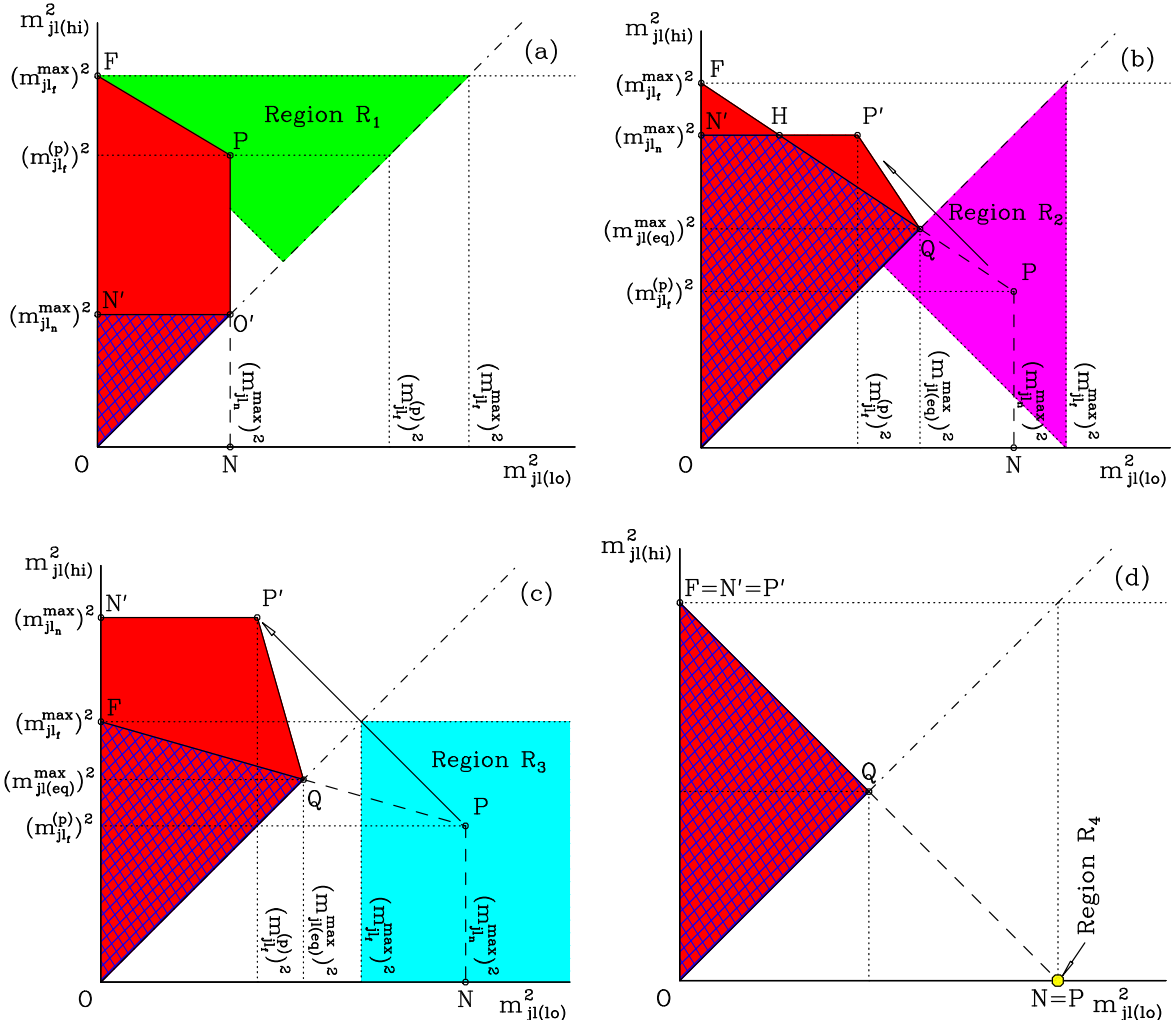


Figure 8: The generic shape of the bivariate distribution $m_{jl(lo)}^2$ versus $m_{jl(hi)}^2$ for each of the four parameter space regions: (a) Region \mathcal{R}_1 , (b) Region \mathcal{R}_2 , (c) Region \mathcal{R}_3 and (d) the off-shell case of Region \mathcal{R}_4 . Each panel shows the typical shape (red-shaded) of the resulting $(m_{jl(lo)}^2, m_{jl(hi)}^2)$ distribution, after the “folding” in Fig. 7. Blue-hatched (unhatched) areas correspond to double-density (single-density) regions. Each panel also shows the original location of the point P in the $(m_{jl_n}^2, m_{jl_f}^2)$ plot, as well as the allowed positions of point P , following the color conventions of Figs. 2 and 6.

characteristic shapes of the $(m_{jl(lo)}^2, m_{jl(hi)}^2)$ distribution for each parameter space region \mathcal{R}_i . Our results are displayed in Fig. 8, where we show the four characteristic shapes for each case: the on-shell cases of (a) Region \mathcal{R}_1 , (b) Region \mathcal{R}_2 , (c) Region \mathcal{R}_3 , and the off-shell case of (d) Region \mathcal{R}_4 . Each panel shows the typical shape (red-shaded) of the resulting $(m_{jl(lo)}^2, m_{jl(hi)}^2)$ distribution, after the “folding” in Fig. 7. Blue-hatched (unhatched) areas correspond to double-density (single-density) regions. In addition, we show the original location of the point P in the $(m_{jl_n}^2, m_{jl_f}^2)$ plot. The allowed positions of point P in each case are color-

shaded, following the color conventions of Figs. 2 and 6.

The nice feature of all the plots in Fig. 8 is that they are composed entirely of straight lines. This is a consequence of the fact that the original trapezoid in Fig. 6 is made up of straight lines, and then the “folding” of Fig. 7 does not curve the boundaries. Notice also the presence of internal kinematic boundaries, marking abrupt changes in the density of the distribution, e.g. $O'N'$ in Fig. 8(a), QHN' in Fig. 8(b) and QF in Fig. 8(c).

It is clear from Fig. 8 that the shape of the $(m_{jl(lo)}^2, m_{jl(hi)}^2)$ scatter plot allows us to uniquely determine the parameter space region at hand. For example, the typical shape for Region \mathcal{R}_1 , exhibited in Fig. 8(a), consists of a right-angle triangular region $OO'N'$ of double density and a right-angle trapezoidal region $N'O'PF$ of single density. In this case, point P is directly observable, and its coordinates immediately yield the quantities n and p defined in (4.3) and (4.5). In addition, one can also measure the location f of point F along the $m_{jl(hi)}^2$ axis, given by eq. (4.4). This gives a total of three independent measurements: n , p and f , which should be ordered as $n < p < f$, in accordance with (4.15). Now we can clearly see the benefit of considering the two-dimensional $(m_{jl(lo)}^2, m_{jl(hi)}^2)$ distribution as opposed to the two individual one-dimensional distributions $m_{jl(lo)}^2$ and $m_{jl(hi)}^2$. Those one-dimensional distributions are obtained by projecting the $(m_{jl(lo)}^2, m_{jl(hi)}^2)$ scatter plot shown in Fig. 8(a) onto the two axes. It is easy to see from Fig. 8(a) that in this case the endpoint of the one-dimensional $m_{jl(lo)}^2$ distribution will be given by $c = n$, while the endpoint of the one-dimensional $m_{jl(hi)}^2$ distribution will be given by $d = f$, and neither of those will reveal the quantity p . In contrast, p can be easily identified on the scatter plot, and provides an additional *independent* measurement.

The case of Region \mathcal{R}_3 , which is shown in Fig. 8(c), is rather similar: the double-density region is still a triangle (OQF), while the single-density region is a quadrilateral ($FQP'N'$). This time instead of point P we can clearly see its image P' , whose coordinates nevertheless still reveal the values of n and p . Point F is now hidden within the scatter plot, but may still be identifiable, since it corresponds to an abrupt change in density of points. Finally, now we have an additional measurement q of point Q , which is where the original line segment FP was folded in the reordering process of eqs. (1.1,1.2). As a result, in region \mathcal{R}_3 we have a total of 4 measurements of kinematic endpoints, n , p , f and q , ordered as follows: $p < q < f < n$ (see also eq. (4.17)). Later, when we project onto the two axes, the endpoint of the one-dimensional $m_{jl(lo)}^2$ distribution will be given by $c = q$, while the endpoint of the one-dimensional $m_{jl(hi)}^2$ distribution will be given by $d = n$. This now leaves out *two* additional potential measurements, p and f , which can be accessed on the two-dimensional scatter plot.

In the third on-shell case of Region \mathcal{R}_2 , shown in Fig. 8(b), the shape is more complex: the double density region is now a quadrilateral $OQHN'$, while there are two disjoint single density triangular regions $QP'H$ and $N'HF$. The point H appears on the intersection of the original FP boundary of the $(m_{jl_n}^2, m_{jl_f}^2)$ scatter plot in Fig. 6 and the (horizontal) image $P'N'$ of the (vertical) PN boundary in Fig. 6. Once again, the coordinates of point P' reveal p and n , while points F and Q reveal f and q , correspondingly. In region \mathcal{R}_2 , therefore, there are 4 potential measurements, p , n , f and q , ordered as follows: $p < q < n < f$. When

the scatter plot of Fig. 8(b) is projected onto the axes, the endpoint of the one-dimensional $m_{jl(lo)}^2$ distribution will be given by $c = q$, while the endpoint of the one-dimensional $m_{jl(hi)}^2$ distribution will be given by $d = f$. Once again, this leaves out *two* additional potential measurements, p and n , which can be extracted from the two-dimensional scatter plot.

Let us now turn to the off-shell scenario of Region \mathcal{R}_4 , which is represented in Fig. 8(d). Because of the symmetry between the “near” and “far” leptons in the off-shell case, the folded region ONQ has an identical triangular shape as the underlying region OFQ , so that after the fold the two match perfectly and we obtain a single triangular region of double density, and no single-density areas. As can be seen from Fig. 8(d), the off-shell scenario offers only one nontrivial endpoint measurement, which can be taken as f . The latter appears as the endpoint d in the one-dimensional $m_{jl(hi)}^2$ distribution, while the endpoint c of the other one-dimensional distribution, $m_{jl(lo)}^2$, is then simply given as $c = f/2$, in agreement with eq. (2.32).

We have just seen that in the off-shell scenario of Fig. 1(b) the two-dimensional scatter plot $(m_{jl(lo)}^2, m_{jl(hi)}^2)$ does not yield any additional kinematic endpoint measurements. However, it can still be helpful in discriminating a potential regional ambiguity which may arise as follows. Notice that the triangular double-density shape of the scatter plot in the off-shell case of Fig. 8(d) can in principle also be obtained in the on-shell cases of Fig. 8(b) and Fig. 8(c), provided that the image P' of point P ends up very close to point F . In terms of the $(m_{jl_n}^2, m_{jl_f}^2)$ scatter plot of Fig. 6, this situation corresponds to the on-shell cases of Regions \mathcal{R}_2 or \mathcal{R}_3 , with point P lying very close to the yellow-shaded dot representing Region \mathcal{R}_4 . In spite of having the same shape of their boundary lines, the two scatter plots will be quite different, as they will exhibit a different point density. In particular, for all three on-shell cases, the pure phase space two-dimensional differential distribution (4.2) is given by the following (unit-normalized) formula

$$\frac{d^2\Gamma}{dm_{jl_n}^2 dm_{jl_f}^2} = \frac{1}{n \left(m_{jl_f}^2 (m_{jl_n}^2) \right)} = \frac{1}{fn - (f-p) m_{jl_n}^2} , \quad (\text{for } R_{BC} < 1). \quad (4.18)$$

Notice that within the kinematically allowed region, the density is independent of $m_{jl_f}^2$. In the limit $p \rightarrow 0$, the expression (4.18) becomes singular when $m_{jl_n}^2 \rightarrow n$. This singularity is regularized by the width of particle B and the branching fraction for the $C \rightarrow B$ decay. In contrast, the corresponding density in the off-shell case is quite different, and in particular does not exhibit such singular features.

We are now ready to revisit the duplication problem discussed in Section 3. We have just seen that the two-dimensional distribution of $m_{jl(lo)}^2$ versus $m_{jl(hi)}^2$ can help resolve the duplication in two very different ways. First, the shape of the kinematic boundary lines in the $(m_{jl(lo)}^2, m_{jl(hi)}^2)$ scatter plot uniquely identifies the region, as shown in Fig. 8. Since the duplicate solutions that we found always appear in two different regions, this is in principle sufficient to eliminate the wrong solution. Secondly, the scatter plots offer the possibility of additional measurements, and at the very least a measurement of the quantity p . As can be seen from Table 2, the value of p is already different for each pair of duplicate spectra, and,

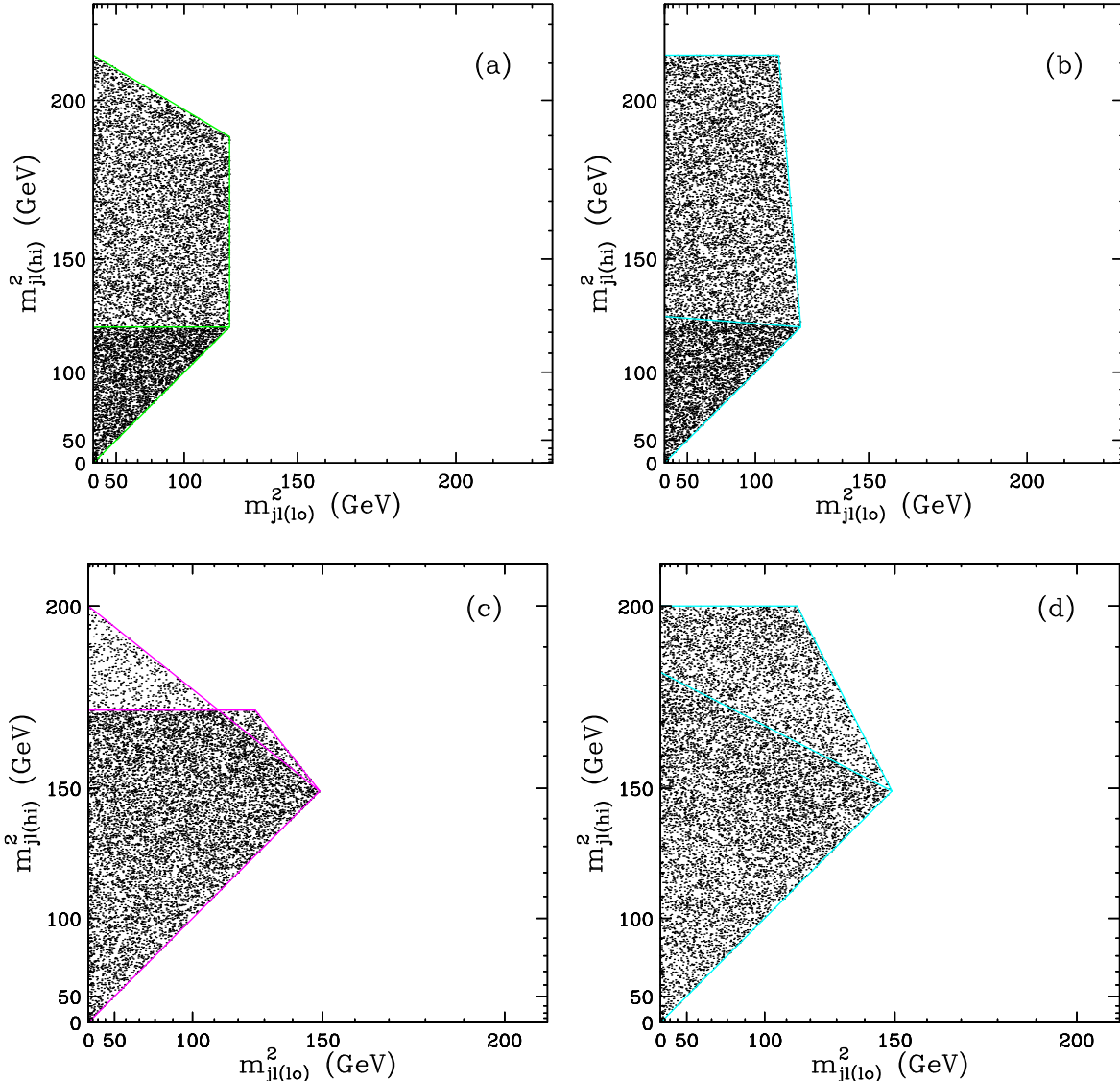


Figure 9: Scatter plots of $m_{jl(lo)}^2$ versus $m_{jl(hi)}^2$ for the four study points from Table 2 exhibiting duplication: (a) point P_{31} , (b) point P_{23} , (c) point P_{32} and (d) point P'_{23} . Notice the quadratic scale used on both axes. The kinematic boundary lines are outlined with the corresponding color for each region, following the color coding conventions of Figs. 2 and 6. Each plot has 10,000 data points. We assume that all particles A , B , C and D are exactly on-shell.

provided that it can be measured with sufficient precision, can also be used to remove the ambiguity.

Our conclusions are confirmed by Fig. 9, which shows the $(m_{jl(lo)}^2, m_{jl(hi)}^2)$ scatter plots for the four study points from Table 2 exhibiting duplication: (a) point P_{31} , (b) point P_{23} , (c) point P_{32} and (d) point P'_{23} . The figure indeed shows that each pair of duplicate points has identical values for the endpoints of the separate *one-dimensional* invariant mass distributions

$m_{jl(lo)}^2$ and $m_{jl(hi)}^2$. However, the shapes of the scatter plots are very different, and so are the values of the corresponding p endpoints. We therefore conclude that the duplication encountered in Section 3 ceases to be a problem, once we generalize the analysis to two-dimensional (bivariate) distributions as discussed here.

In conclusion of this section, we point out that when the two-dimensional scatter plots like those in Fig. 9 are projected onto the axes to obtain the corresponding one-dimensional distributions of either $m_{jl(lo)}^2$ or $m_{jl(hi)}^2$, the latter often exhibit some peculiar features near their endpoints, which were classified as either “feet” or “drops” in ref. [30]. The origin of these features is now easy to understand in terms of the original two-dimensional scatter plot. For example, consider the scatter plots in Figs. 9(b) and 9(d). When projected onto the $m_{jl(hi)}^2$ axis, both of them will exhibit a classic “drop” at the $m_{jl(hi)}^2$ endpoint, which is simply due to the flat upper boundary $P'N'$ in Fig. 8(c). Similarly, the projection of the scatter plot in Fig. 9(c) onto the $m_{jl(hi)}^2$ axis will exhibit a classic “foot” extending from n to f . The “foot” can be easily understood in terms of the generic shape of Fig. 8(b), where it arises from the projection of the single density area $N'HF$.

5. Kinematic boundary lines for the m_{ll}^2 vs. m_{jll}^2 distribution

Following the logic of the previous section, we shall now proceed to analyze the two-dimensional distribution

$$\frac{d^2\Gamma}{dm_{jll}^2 dm_{ll}^2}, \quad (5.1)$$

whose generic shape $OVUS$ is shown in Fig. 10. The kinematic boundary lines of the scatter plot (5.1) generally consist of four segments. The upper (SU) and lower (OV) curved boundaries are parts of a hyperbolic curve OWS , while the left (OS) and right (UV) boundaries are straight lines. Therefore, in order to describe the shape of the (m_{ll}^2, m_{jll}^2) scatter plot, it is sufficient to provide the parametric equations for the upper and lower curved boundaries SW and OW , plus the location of the vertical line UV . In analogy with (4.9), we choose the variable on the horizontal axis, in this case m_{ll}^2 , as the line parameter describing the hyperbola OWS . Then the upper boundary line SUW is given by the parametric equation [33]

$$\begin{aligned} m_{jll(+)}^2(m_{ll}^2) &= \frac{1+R_{CD}}{2} \frac{m_{ll}^2}{R_{CD}} + \frac{1}{2} m_D^2 (1-R_{CD})(1-R_{AC}) \\ &+ \frac{1-R_{CD}}{2} \left\{ \left[\left(\frac{m_{ll}^2}{R_{CD}} \right) - m_D^2 (1+R_{AC}) \right]^2 - 4m_D^4 R_{AC} \right\}^{\frac{1}{2}}, \end{aligned} \quad (5.2)$$

while the lower boundary line OVW is given by [33]

$$\begin{aligned} m_{jll(-)}^2(m_{ll}^2) &= \frac{1+R_{CD}}{2} \frac{m_{ll}^2}{R_{CD}} + \frac{1}{2} m_D^2 (1-R_{CD})(1-R_{AC}) \\ &- \frac{1-R_{CD}}{2} \left\{ \left[\left(\frac{m_{ll}^2}{R_{CD}} \right) - m_D^2 (1+R_{AC}) \right]^2 - 4m_D^4 R_{AC} \right\}^{\frac{1}{2}}. \end{aligned} \quad (5.3)$$

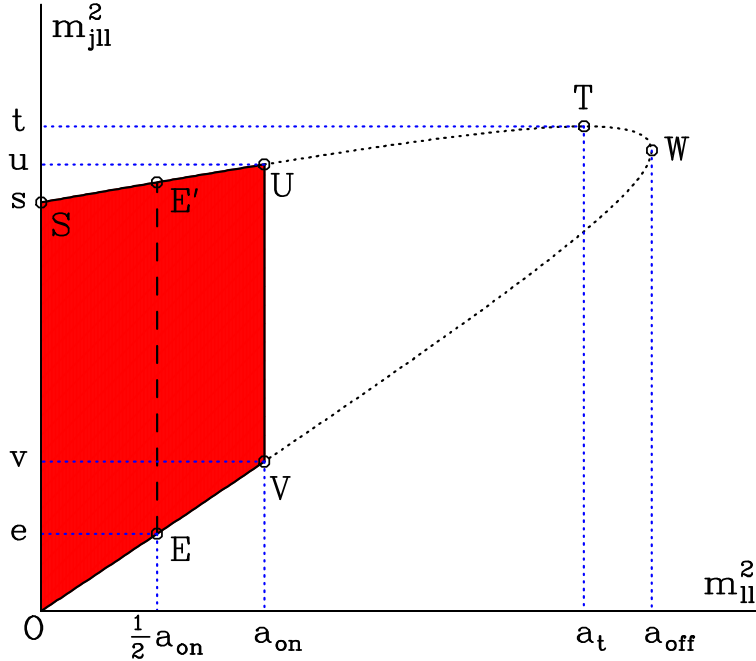


Figure 10: The generic shape $OVUS$ of the bivariate distribution (5.1) in the (m_{ll}^2, m_{jll}^2) plane.

The vertical straight line segment UV is in general located at $m_{ll}^2 = a$, where a is the value of the dilepton invariant mass endpoint $(m_{ll}^{max})^2$ already introduced in Section 2.1. As we saw in Section 2.1, the expression for $a = (m_{ll}^{max})^2$ depends on whether we are dealing with the on-shell scenario of Fig. 1(a) or the off-shell scenario of Fig. 1(b). Therefore we shall now introduce separate notation for the endpoint a in each of these two cases. In the on-shell scenario of Fig. 1(a) we shall use a_{on} to designate our previous eq. (2.8)

$$a_{\text{on}} \equiv m_D^2 R_{CD} (1 - R_{BC}) (1 - R_{AB}), \quad (5.4)$$

while in the off-shell scenario of Fig. 1(b) we shall use a_{off} for the previous result (2.18)

$$a_{\text{off}} \equiv m_D^2 R_{CD} (1 - \sqrt{R_{AC}})^2. \quad (5.5)$$

From these two equations, it is not difficult to see that

$$a_{\text{on}} \leq a_{\text{off}}, \quad (5.6)$$

as indicated in Fig. 10. As an aside, we mention that with the help of eqs. (5.4) and (5.5) it is easy to show that the equal sign in (5.6) is achieved when $R_{AB} = R_{BC}$, i.e. when the on-shell spectrum happens to lie exactly on the border between regions \mathcal{R}_2 and \mathcal{R}_3 in Fig. 2. In physical terms this means that the mass m_B of particle B is equal to the geometric mean of m_A and m_C :

$$m_B = \sqrt{m_A m_C} \quad \Rightarrow \quad a_{\text{on}} = a_{\text{off}}. \quad (5.7)$$

This represents another potential source of confusion in extracting the mass spectrum – the measurement of the dilepton invariant mass endpoint a alone tells us nothing about

whether the intermediate particle B is on-shell or off-shell, leading to two possible solutions [28]. Fortunately, with the inclusion of the additional measurements c , d and e , we did not encounter this type of duplication in the course of our analysis in Sec. 3.

Returning now to our discussion of the (m_{ll}^2, m_{jll}^2) scatter plot in Fig. 10, eq. (5.6) implies that in the on-shell case of Fig. 1(a), the data points do not fill up the whole region OWS , but only extend up to the vertical boundary UV . The region to the right of the UV line is kinematically inaccessible. On the other hand, in the off-shell case of Fig. 1(b), the whole region OWS is filled up. The only exception to this rule is the very special on-shell case of (5.7), when the UV line moves to the very tip W of the hyperbola, thus allowing the whole region OWS , as if this were an off-shell scenario.

In analogy with our discussion in Section 4 of the kinematic boundaries in the two-dimensional $(m_{jl(l)}^2, m_{jl(h)}^2)$ distribution, we now identify several special points along the hyperbola OWS in Fig. 10. Point O is simply the origin $(0, 0)$ of the (m_{ll}^2, m_{jll}^2) coordinate system. Point W is the tip of the hyperbola, where the upper branch $m_{jll(+)}^2(m_{ll}^2)$ meets the lower branch $m_{jll(-)}^2(m_{ll}^2)$. By definition, the m_{ll}^2 coordinate of point W is a_{off} , while its m_{jll}^2 coordinate is

$$w \equiv m_{jll(+)}^2(a_{\text{off}}) \equiv m_{jll(-)}^2(a_{\text{off}}) = m_D^2 \left(1 - R_{CD} \sqrt{R_{AC}}\right) \left(1 - \sqrt{R_{AC}}\right). \quad (5.8)$$

Point S is where the upper kinematic boundary line $m_{jll(+)}^2(m_{ll}^2)$ intersects the m_{jll}^2 coordinate axis. The m_{jll}^2 coordinate of point S is therefore

$$s \equiv m_{jll(+)}^2(0) = m_D^2 (1 - R_{CD}) (1 - R_{AC}). \quad (5.9)$$

Points U and V label the intersections of the vertical boundary UV with the upper and lower hyperbolic branches (5.2) and (5.3), respectively. They share the same m_{ll}^2 coordinate a_{on} , while their m_{jll}^2 coordinates are correspondingly given by

$$u \equiv m_{jll(+)}^2(a_{\text{on}}) \quad (5.10)$$

$$= \frac{1}{2} m_D^2 \left[(1 + R_{CD})(1 - R_{BC})(1 - R_{AB}) + (1 - R_{CD})(1 - R_{AC} + |R_{BC} - R_{AB}|) \right],$$

$$v \equiv m_{jll(-)}^2(a_{\text{on}}) \quad (5.11)$$

$$= \frac{1}{2} m_D^2 \left[(1 + R_{CD})(1 - R_{BC})(1 - R_{AB}) + (1 - R_{CD})(1 - R_{AC} - |R_{BC} - R_{AB}|) \right].$$

Finally, there is one more special point on the upper branch SUW : it is the point T where $m_{jll(+)}^2(m_{ll}^2)$ has a local maximum. The m_{ll}^2 coordinate a_t of point T can be found from the minimization condition

$$\left(\frac{dm_{jll(+)}^2}{dm_{ll}^2} \right)_{m_{ll}^2=a_t} = 0 \quad (5.12)$$

and is given by

$$a_t \equiv m_D^2 \left(R_{CD} - \sqrt{R_{AD}} \right) \left(1 - \sqrt{R_{AD}} \right). \quad (5.13)$$

Then, the m_{jll}^2 coordinate t of point T is easily found by substituting (5.13) into (5.2):

$$t \equiv m_{jll(+)}^2(a_t) = m_D^2 \left(1 - \sqrt{R_{AD}}\right)^2. \quad (5.14)$$

We should point out that point T as we have defined it here, does not exist in all parameter space regions. To see this, let us calculate the slope of the upper branch $m_{jll(+)}^2(m_{ll}^2)$ at point S :

$$\left(\frac{dm_{jll(+)}^2}{dm_{ll}^2}\right)_{m_{ll}^2=0} = \frac{R_{CD} - R_{AC}}{R_{CD}(1 - R_{AC})}. \quad (5.15)$$

Since the denominator is always positive, the sign of the derivative is determined by the relative size of R_{CD} and R_{AC} . When $R_{CD} < R_{AC}$, the slope is negative, and T does not exist. In that case, the maximum value of m_{jll}^2 over the whole scatter plot $OVUS$ is obtained exactly at S , and is given by s in eq. (5.9). Comparing to the first lines in eqs. (2.9) and (2.19), we see that this happens precisely for the cases of $N_{jll} = 1$ and $N_{jll} = 5$. In contrast, for the other four cases $N_{jll} = 2, 3, 4, 6$, the slope at point S is positive and point T is well defined. However, this does not mean that point T would then necessarily belong to the scatter plot $OVUS$. In the off-shell case of $N_{jll} = 6$, point T clearly belongs to the scatter plot, and the maximum value of m_{jll}^2 is given by t in eq. (5.14), in agreement with the second line in eq. (2.19). However, in the remaining three on-shell cases $N_{jll} = 2, 3, 4$ one has to be more careful. Since the scatter plot is then limited by the UV vertical boundary, point T will be included only if it lies to the left of the UV line, i.e. we must have

$$a_t < a_{\text{on}}. \quad (5.16)$$

Using (5.13) and (5.4), this condition can be equivalently rewritten as

$$(R_{BC} - R_{AB}R_{CD})(R_{AB} - R_{BD}) > 0. \quad (5.17)$$

Alternatively, the point T will fall outside the scatter plot, whenever

$$a_t > a_{\text{on}}, \quad (5.18)$$

or equivalently,

$$(R_{BC} - R_{AB}R_{CD})(R_{AB} - R_{BD}) < 0. \quad (5.19)$$

We see that whether point T is included or not, depends on the sign of the expression

$$(R_{BC} - R_{AB}R_{CD})(R_{AB} - R_{BD}). \quad (5.20)$$

Notice that the two factors entering this expression cannot be simultaneously negative: if that were the case, we would have

$$\left. \begin{aligned} R_{BC} - R_{AB}R_{CD} &< 0 \Rightarrow m_B^2 < \frac{m_A}{m_D} m_C^2 \\ R_{AB} - R_{BD} &< 0 \Rightarrow m_A m_D < m_B^2 \end{aligned} \right\} \Rightarrow m_D < m_C, \quad (5.21)$$

which contradicts our basic assumption (2.6). Therefore, whenever one of the two factors in (5.20) is negative, the other is guaranteed to be positive. Of course, it is also possible that both factors in (5.20) are positive to begin with. Altogether, this leads to three different possibilities, which are related to the $N_{jll} = 2, 3, 4$ cases of eq. (2.9).

- $N_{jll} = 2$. In this case, the first factor in eq. (5.20) is negative, leading to the following logical chain

$$\begin{aligned} N_{jll} = 2 : R_{BC} - R_{AB}R_{CD} < 0 &\Rightarrow R_{AB} - R_{BD} > 0 \\ &\Rightarrow (R_{BC} - R_{AB}R_{CD})(R_{AB} - R_{BD}) < 0 \Rightarrow a_t > a_{\text{on}}, \end{aligned} \quad (5.22)$$

placing point T outside the scatter plot. Then, the maximum value of m_{jll}^2 is obtained at point U and is given by eq. (5.10). Since in this case $R_{BC} < R_{AB}R_{CD} < R_{AB}$, the absolute value sign in (5.10) can be resolved as $|R_{BC} - R_{AB}| = R_{AB} - R_{BC}$ and then eq. (5.10) simplifies to

$$u = m_D^2(1 - R_{BC})(1 - R_{AB}R_{CD}), \quad (5.23)$$

confirming the result on the second line of eq. (2.9).

- $N_{jll} = 3$. In this case, it is the second factor in eq. (5.20) which is negative:

$$\begin{aligned} N_{jll} = 3 : R_{AB} - R_{BD} < 0 &\Rightarrow R_{BC} - R_{AB}R_{CD} > 0 \\ &\Rightarrow (R_{BC} - R_{AB}R_{CD})(R_{AB} - R_{BD}) < 0 \Rightarrow a_t > a_{\text{on}}. \end{aligned} \quad (5.24)$$

Once again, point T is outside the scatter plot, and the maximum value of m_{jll}^2 is obtained at point U and is given by (5.10). This time, however, $R_{AB} < R_{BD} = R_{BC}R_{CD} < R_{BC}$, and correspondingly, $|R_{BC} - R_{AB}| = R_{BC} - R_{AB}$. Then, eq. (5.10) simplifies to

$$u = m_D^2(1 - R_{AB})(1 - R_{BD}), \quad (5.25)$$

agreeing with the third line of eq. (2.9).

- $N_{jll} = 4$. This is the case when both factors in eq. (5.20) are positive, leading to

$$N_{jll} = 4 : \left. \begin{aligned} R_{BC} - R_{AB}R_{CD} &> 0 \\ R_{AB} - R_{BD} &> 0 \end{aligned} \right\} \Rightarrow (R_{BC} - R_{AB}R_{CD})(R_{AB} - R_{BD}) > 0 \Rightarrow a_t < a_{\text{on}}. \quad (5.26)$$

Point T now belongs to the scatter plot, and its coordinate t defined in (5.14) gives the maximum value of the m_{jll}^2 distribution, in agreement with the fourth line of (2.9).

Note that Fig. 10 now allows us to understand geometrically the physical meaning of the *lower* threshold $e = (m_{jll}^{\min}(\theta > \frac{\pi}{2}))^2$ introduced in Section 2. If we restrict ourselves only to points with $m_{jll}^2 > \frac{1}{2}a_{\text{on}}$, i.e. to the right of the dashed line EE' , the one-dimensional m_{jll}^2

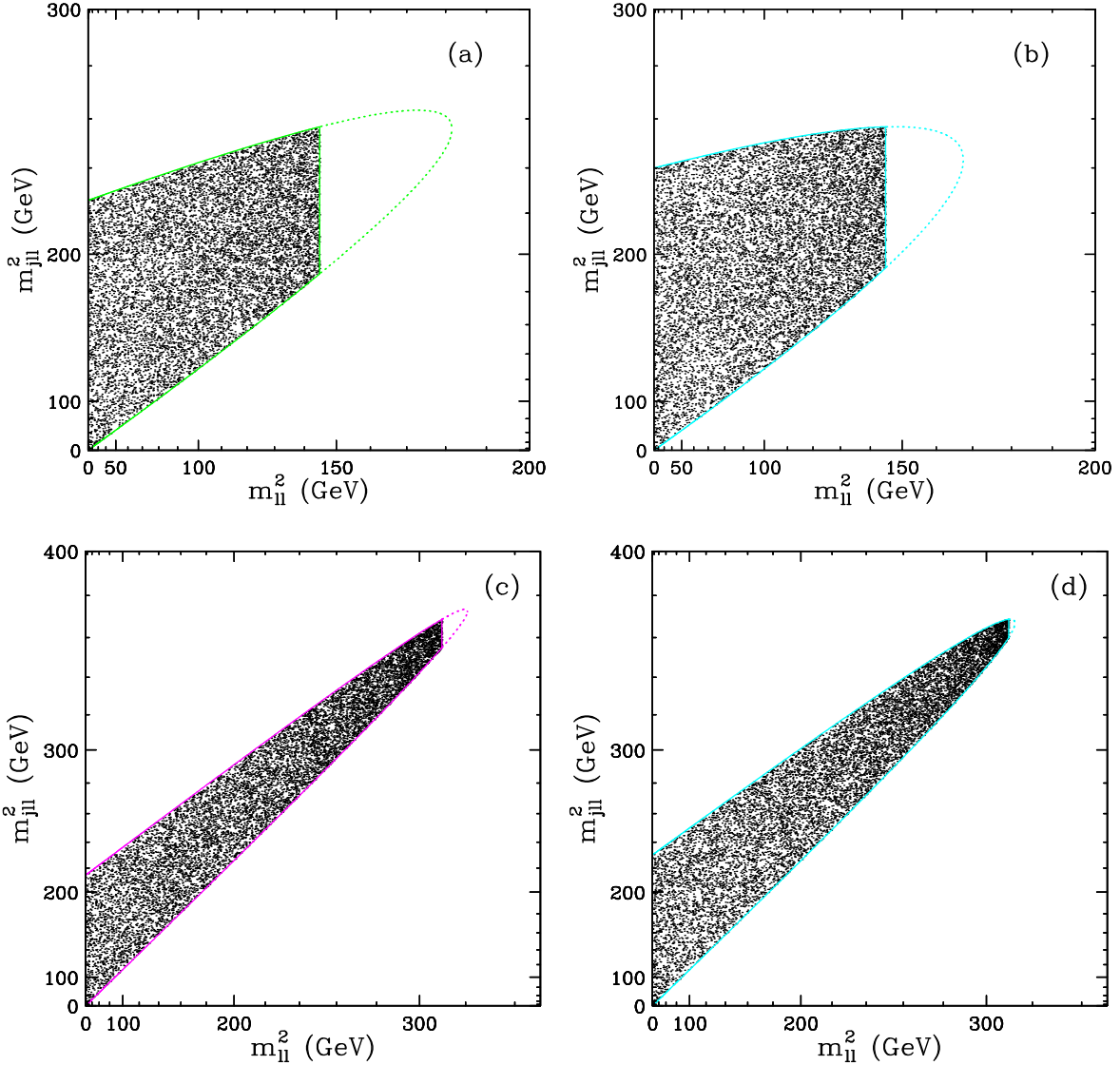


Figure 11: The same as Fig. 9, but for m_{ll}^2 versus m_{jll}^2 .

distribution will exhibit a *lower* endpoint, whose value e is given by the m_{jll}^2 coordinate of point E in Fig. 10. In the on-shell case, e is given by

$$\begin{aligned}
 e \equiv m_{jll(-)}^2(a_{\text{on}}/2) &= \frac{1}{4}m_D^2 \left\{ (1 + R_{CD})(1 - R_{AB})(1 - R_{BC}) \right. \\
 &\quad \left. + 2(1 - R_{CD})(1 - R_{AC}) - (1 - R_{CD})\sqrt{(1 + R_{AB})^2(1 + R_{BC})^2 - 16R_{AC}} \right\}, \tag{5.27}
 \end{aligned}$$

while in the off-shell case e is given by

$$e \equiv m_{jll(-)}^2(a_{\text{off}}/2) = \frac{1}{4}m_D^2(1 - \sqrt{R_{AC}}) \left\{ 2R_{CD}(1 - \sqrt{R_{AC}}) \right. \\ \left. + (1 - R_{CD}) \left(3 + \sqrt{R_{AC}} - \sqrt{1 + R_{AC} + 6\sqrt{R_{AC}}} \right) \right\}. \quad (5.28)$$

It is not difficult to see that eqs. (5.27) and (5.28) are identical to (2.15) and (2.22), correspondingly.

The newly introduced quantities s , t , u and v can be directly observed experimentally¹² on the scatter plot of Fig. 10. Table 2 lists their square root values for our four duplicate study points P_{31} , P_{23} , P_{32} and P'_{23} . As expected, the value of u is matched identically for each pair. However, the two other directly observable quantities s and v differ, and in principle can be used to resolve the duplication. This is illustrated in Fig. 11, where we plot the two-dimensional distribution (5.1) for each duplicated example: (a) P_{31} , (b) P_{23} , (c) P_{32} and (d) P'_{23} . Unlike Fig. 9, here the differences between the scatter plots for each duplicated pair are only quantitative, and may be difficult to observe in practice. The fact that the plots look similar is not very surprising, given our earlier discussion. Notice that duplication occurs only in regions with $N_{jll} = 2$ or $N_{jll} = 3$. In both cases, the shape of the (m_{ll}^2, m_{jll}^2) scatter plot is rather similar: the slope at point S is positive, and the upper boundary SU is cut off before it reaches the local maximum at point T . Furthermore, the duplication analysis ensures that the rightmost vertical boundary UV occurs in the same location a_{on} .

6. Summary and outlook

We now summarize the main results of the paper and discuss possible directions for future investigations. Our main results are as follows:

- In Section 2.2 we provided analytical inversion formulas which allow the immediate calculation of the mass spectrum m_A , m_B , m_C and m_D in terms of a set of four measured invariant mass endpoints $\{a, c, d, e\}$. Our formulas are valid in *all* parameter space regions, since we do not use the endpoint $b = m_{jll}^{\max}$, which is problematic in regions (3,1), (3,2) and (2,3), see eq. (2.17).
- Once the endpoint m_{jll}^{\max} is eliminated from the discussion, we only need to consider 4 different cases, \mathcal{R}_i , $i = 1, 2, 3, 4$, as illustrated with the color-coded regions in Fig. 2. In contrast, previous studies which made use of the m_{jll}^{\max} endpoint [26, 27, 30] were forced to consider all 11 different possibilities (N_{jll}, N_{jl}) shown in Fig. 2.

¹²In principle, one can also measure indirectly the locations of points W and T , even when they fall outside the observable scatter plot. Since the analytical expressions (5.2) and (5.3) for the boundary lines are already known, one can fit them to the observable portions on the scatter plot, and then extrapolate the obtained analytical fit into the kinematically inaccessible region, thus obtaining the “would-be” positions of T and W .

- We investigated analytically the possibility of finding multiple solutions for the mass spectrum, even when a perfect experiment can measure the values for *all five* invariant mass endpoints $\{a, b, c, d, e\}$ with zero error bars. Although we still had to consider separately each of the four different cases \mathcal{R}_i , we found that in most of the parameter space the spectrum is uniquely determined. Unfortunately, there is also a certain portion of parameter space, illustrated in Fig. 5, where one finds an exact duplication, i.e. two very different mass spectra yield identical values for all five measurements $\{a, b, c, d, e\}$. The situation is only going to get worse, once we take into account the inevitable experimental errors on the endpoint measurements, which can only proliferate the number of candidate solutions. Our results show that the conventional method of invariant mass endpoints may not be sufficient and one needs to look for new fresh ideas.
- The main goal of this paper is to advertise a new approach to the study of the usual invariant mass distributions. In particular, we point out that the multivariate invariant mass distributions contain a lot more useful information than the individual one-dimensional histograms, which are usually considered. As two illustrative examples, we discussed the two-dimensional $\{m_{j\ell(lo)}^2, m_{j\ell(hi)}^2\}$ distribution in Section 4 and the two-dimensional $\{m_{\ell\ell}^2, m_{j\ell\ell}^2\}$ distribution in Section 5. The former is always bounded by straight lines (see Fig. 8), while the latter is bounded by the hyperbola given by (5.2) and (5.3), and (in the on-shell case only) by the straight line UV in Fig. 10.
- The two-dimensional distributions exhibit two useful features. First, their shapes, i.e. the locations and orientations of their boundary lines, are characteristic of the corresponding parameter space region \mathcal{R}_i , as shown in Figs. 8 and 10. This observation can be used to identify the relevant parameter space region, and resolve potential ambiguities in the extraction of the mass spectrum. Second, the boundary lines exhibit a number of special points, whose coordinates can in principle be measured, providing additional experimental information about the mass spectrum. For example, in the $\{m_{j\ell(lo)}^2, m_{j\ell(hi)}^2\}$ scatter plots of Fig. 8 one may identify points F, P, N and Q , and correspondingly measure their $m_{j\ell(hi)}^2$ coordinates, which (in the on-shell case) are given by

$$f = m_D^2 (1 - R_{CD}) (1 - R_{AB}), \quad (6.1)$$

$$p = m_D^2 (1 - R_{CD}) R_{BC} (1 - R_{AB}), \quad (6.2)$$

$$n = m_D^2 (1 - R_{CD}) (1 - R_{BC}), \quad (6.3)$$

$$q = m_D^2 (1 - R_{CD}) \frac{1 - R_{AB}}{2 - R_{AB}}. \quad (6.4)$$

Similarly, on the $\{m_{\ell\ell}^2, m_{j\ell\ell}^2\}$ scatter plot in Fig. 10 one may identify the points $S, U,$

V , E , and (sometimes) T and W . Their m_{jll}^2 coordinates are given by

$$s = m_D^2 (1 - R_{CD}) (1 - R_{AC}), \quad (6.5)$$

$$u = \frac{1}{2} m_D^2 \left[(1 + R_{CD})(1 - R_{BC})(1 - R_{AB}) \right. \\ \left. + (1 - R_{CD})(1 - R_{AC} + |R_{BC} - R_{AB}|) \right], \quad (6.6)$$

$$v = \frac{1}{2} m_D^2 \left[(1 + R_{CD})(1 - R_{BC})(1 - R_{AB}) \right. \\ \left. + (1 - R_{CD})(1 - R_{AC} - |R_{BC} - R_{AB}|) \right], \quad (6.7)$$

$$e = \frac{1}{4} m_D^2 \left[(1 + R_{CD})(1 - R_{AB})(1 - R_{BC}) + 2(1 - R_{CD})(1 - R_{AC}) \right. \\ \left. - (1 - R_{CD})\sqrt{(1 + R_{AB})^2(1 + R_{BC})^2 - 16R_{AC}} \right], \quad (6.8)$$

$$t = m_D^2 \left(1 - \sqrt{R_{AD}} \right)^2, \quad (6.9)$$

$$w = m_D^2 \left(1 - R_{CD}\sqrt{R_{AC}} \right) \left(1 - \sqrt{R_{AC}} \right). \quad (6.10)$$

The advantage of the new approach is apparent from eqs. (6.1-6.10). Including the dilepton invariant mass endpoint a , the set of potential invariant mass endpoint measurements has now expanded to 11:

$$\{a, f, p, n, q, s, u, v, e, t, w\} \quad (6.11)$$

instead of the original five:

$$\{a, b, c, d, e\}. \quad (6.12)$$

Of course, the endpoints in (6.11) are not independent from each other, since they are all given in terms of only 4 input parameters (2.7). Nevertheless, it is certainly preferable to have as many measurements as possible. The redundancy of information is a virtue, since it helps to improve the precision of the mass determination.

- The inversion formulas may simplify considerably, if we replace e , whose analytical expression (6.8) is rather complicated, with some of the other measurements in (6.1-6.10). One such example is shown in Appendix A, where we start from the set $\{a, f, p, n\}$, and obtain a very simple result (A.11-A.14) for the inversion.
- An important advantage of the two-dimensional approach is that one can readily resolve the ambiguity between the endpoints of the m_{jlf}^2 and the m_{jln}^2 distributions. Indeed, notice that the endpoints (6.1) and (6.3), are region-independent, and can be directly observed from the boundary lines. This removes the need to consider the different

parameter space regions \mathcal{R}_i one by one. The possibility of distinguishing the jl_n and jl_f invariant mass endpoints from two-dimensional scatter plots was also suggested in Refs. [88] and [89], where the $\{m_{ll}^2, m_{jl}^2\}$ distribution was used instead.

- Another advantage of the two-dimensional representation of the data is that one can then perform a fit to the boundary lines of the scatter plot instead of a fit to the endpoints in the one-dimensional distributions. This improves the precision of the mass determination, as demonstrated in [89] for the SPS1a SUSY benchmark example.

In conclusion, we outline several directions for future investigations.

- ★ Perhaps the most pressing question is whether and how well the method proposed here will survive the experimental complications of a full-blown analysis including detector simulation, backgrounds from Standard Model as well as SUSY combinatorics, the finite widths of the particles B , C and D , the varying population density of the scatter plots, etc. This is currently under study in the CMS SUSY working group and results will be presented in a separate publication.
- ★ In this paper we limited ourselves to the analysis of the boundary *lines* of two-dimensional distributions. However, the method can be easily generalized by including one more dimension and studying the boundary *surface* of the three-dimensional distribution (1.9). A similar generalization was already shown to be beneficial in the case of spin measurements [69].
- ★ One could also consider other choices of two-dimensional distributions, for example $\{m_{ll}^2, m_{jl}^2\}$, $\{m_{jl}^2, m_{jl}^2\}$ [88], or $\{m_{ll}^2, m_{jl(l)}^2\}$, $\{m_{ll}^2, m_{jl(h)}^2\}$ [89]. Those distributions also allow to discriminate between the “near” and “far” lepton endpoints, and will contribute even more data points to the set (6.11).
- ★ One could also generalize the method to a longer decay chain, e.g. one which starts with a gluino [27].

Acknowledgments

We thank A. Barr, H.-C. Cheng, P. Konar, K. Kong, C. Lester, F. Moortgat, M. Nojiri, L. Pape and M. Peskin for useful discussions. This work is supported in part by a US Department of Energy grant DE-FG02-97ER41029.

A. Appendix: Simple inversion formulas in regions \mathcal{R}_1 , \mathcal{R}_2 and \mathcal{R}_3

In Sec. 4 have saw that the shape analysis of a $(m_{jl(l)}^2, m_{jl(h)}^2)$ scatter plot alone reveals the values of

$$f \equiv (m_{jl_f}^{max})^2 = m_D^2(1 - R_{CD})(1 - R_{AB}), \quad (\text{A.1})$$

$$p \equiv \left(m_{jl_f}^{(p)} \right)^2 = m_D^2 R_{BC} (1 - R_{CD}) (1 - R_{AB}) = f R_{BC}, \quad (\text{A.2})$$

$$n \equiv (m_{jl_n}^{max})^2 = m_D^2 (1 - R_{CD}) (1 - R_{BC}), \quad (\text{A.3})$$

in each of the three on-shell regions \mathcal{R}_1 , \mathcal{R}_2 and \mathcal{R}_3 . In addition, in regions \mathcal{R}_2 and \mathcal{R}_3 one also has a fourth measurement

$$q \equiv \left(m_{jl(ea)}^{max} \right)^2 = m_D^2 (1 - R_{CD}) \frac{1 - R_{AB}}{2 - R_{AB}}. \quad (\text{A.4})$$

Given these four measurements, it is worth asking whether the spectrum of four masses m_A , m_B , m_C and m_D can be uniquely determined based on the $(m_{jl(l_o)}^2, m_{jl(h_i)}^2)$ scatter plot alone. Unfortunately, this is not possible, since the four measurements f , p , n and q are not all independent, due to the constraint (4.8). Therefore, one more independent measurement is needed.

Fortunately, the dilepton mass edge measurement is both robust and on-shell-region-independent. Thus adding

$$a \equiv (m_{ll}^{max})^2 = m_D^2 R_{CD} (1 - R_{BC}) (1 - R_{AB}), \quad (\text{A.5})$$

we obtain a set of 4 measurements

$$\{a, f, p, n\} \equiv \{(m_{jl_f}^{max})^2, (m_{jl_f}^{(p)})^2, (m_{jl_n}^{max})^2, (m_{ll}^{max})^2\}, \quad (\text{A.6})$$

which can be easily inverted to obtain the spectrum:

$$R_{AB} = 1 - \frac{f - p}{n}, \quad (\text{A.7})$$

$$R_{BC} = \frac{p}{f}, \quad (\text{A.8})$$

$$R_{CD} = \left(1 + \frac{f - p}{a} \right)^{-1}, \quad (\text{A.9})$$

$$m_D^2 = \frac{a f n}{(f - p)^2} \left(1 + \frac{f - p}{a} \right). \quad (\text{A.10})$$

In terms of the actual masses we get

$$m_A^2 = \frac{a n p}{(f - p)^2} \left(1 - \frac{f - p}{n} \right), \quad (\text{A.11})$$

$$m_B^2 = \frac{a n p}{(f - p)^2}, \quad (\text{A.12})$$

$$m_C^2 = \frac{a n f}{(f - p)^2}, \quad (\text{A.13})$$

$$m_D^2 = \frac{a n f}{(f - p)^2} \left(1 + \frac{f - p}{a} \right). \quad (\text{A.14})$$

Notice the simplicity of these formulas in comparison to (2.23-2.26) and (2.28-2.30). The simplicity is mostly due to the fact that we are not using the measurement (2.15) whose analytical expression is rather complicated.

References

- [1] For a recent review, see G. Bertone, D. Hooper and J. Silk, “Particle dark matter: Evidence, candidates and constraints,” *Phys. Rept.* **405**, 279 (2005) [arXiv:hep-ph/0404175].
- [2] See, for example, J. Hubisz, J. Lykken, M. Pierini and M. Spiropulu, “Missing energy look-alikes with 100 pb-1 at the LHC,” arXiv:0805.2398 [hep-ph], and references therein.
- [3] A. Birkedal, K. Matchev and M. Perelstein, “Dark matter at colliders: A model-independent approach,” *Phys. Rev. D* **70**, 077701 (2004) [arXiv:hep-ph/0403004].
- [4] J. L. Feng, S. Su and F. Takayama, “Lower limit on dark matter production at the Large Hadron Collider,” *Phys. Rev. Lett.* **96**, 151802 (2006) [arXiv:hep-ph/0503117].
- [5] P. Konar, K. Kong, K. T. Matchev and M. Perelstein, “Shedding Light on the Dark Sector with Direct WIMP Production,” arXiv:0902.2000 [hep-ph].
- [6] For a recent review on supersymmetry phenomenology, see D. J. H. Chung, L. L. Everett, G. L. Kane, S. F. King, J. D. Lykken and L. T. Wang, “The soft supersymmetry-breaking Lagrangian: Theory and applications,” *Phys. Rept.* **407**, 1 (2005) [arXiv:hep-ph/0312378].
- [7] T. Appelquist, H. C. Cheng and B. A. Dobrescu, “Bounds on universal extra dimensions,” *Phys. Rev. D* **64**, 035002 (2001) [arXiv:hep-ph/0012100].
- [8] H. C. Cheng, K. T. Matchev and M. Schmaltz, “Radiative corrections to Kaluza-Klein masses,” *Phys. Rev. D* **66**, 036005 (2002) [arXiv:hep-ph/0204342].
- [9] H. C. Cheng, K. T. Matchev and M. Schmaltz, “Bosonic supersymmetry? Getting fooled at the LHC,” *Phys. Rev. D* **66**, 056006 (2002) [arXiv:hep-ph/0205314].
- [10] K. Agashe and G. Servant, “Warped unification, proton stability and dark matter,” *Phys. Rev. Lett.* **93**, 231805 (2004) [arXiv:hep-ph/0403143].
- [11] K. Agashe, A. Falkowski, I. Low and G. Servant, “KK Parity in Warped Extra Dimension,” *JHEP* **0804**, 027 (2008) [arXiv:0712.2455 [hep-ph]].
- [12] G. Panico, E. Ponton, J. Santiago and M. Serone, “Dark Matter and Electroweak Symmetry Breaking in Models with Warped Extra Dimensions,” *Phys. Rev. D* **77**, 115012 (2008) [arXiv:0801.1645 [hep-ph]].
- [13] H. C. Cheng and I. Low, “TeV symmetry and the little hierarchy problem,” *JHEP* **0309**, 051 (2003) [arXiv:hep-ph/0308199].
- [14] H. C. Cheng and I. Low, “Little hierarchy, little Higgses, and a little symmetry,” *JHEP* **0408**, 061 (2004) [arXiv:hep-ph/0405243].
- [15] I. Hinchliffe, F. E. Paige, M. D. Shapiro, J. Soderqvist and W. Yao, “Precision SUSY measurements at LHC,” *Phys. Rev. D* **55**, 5520 (1997) [arXiv:hep-ph/9610544].
- [16] C. G. Lester and D. J. Summers, “Measuring masses of semi-invisibly decaying particles pair produced at hadron colliders,” *Phys. Lett. B* **463**, 99 (1999) [arXiv:hep-ph/9906349].
- [17] H. Bachacou, I. Hinchliffe and F. E. Paige, “Measurements of masses in SUGRA models at LHC,” *Phys. Rev. D* **62**, 015009 (2000) [arXiv:hep-ph/9907518].
- [18] I. Hinchliffe and F. E. Paige, “Measurements in SUGRA models with large tan(beta) at LHC,” *Phys. Rev. D* **61**, 095011 (2000) [arXiv:hep-ph/9907519].

- [19] ATLAS collaboration, *ATLAS detector and physics performance*, ATLAS TDR 15, CERN/LHCC 99-15
- [20] M. M. Nojiri, D. Toya and T. Kobayashi, “Lepton Energy Asymmetry and Precision SUSY study at Hadron Colliders,” *Phys. Rev. D* **62**, 075009 (2000) [arXiv:hep-ph/0001267].
- [21] B. C. Allanach, C. G. Lester, M. A. Parker and B. R. Webber, “Measuring sparticle masses in non-universal string inspired models at the LHC,” *JHEP* **0009**, 004 (2000) [arXiv:hep-ph/0007009].
- [22] A. Barr, C. Lester and P. Stephens, “ $m(T2)$: The truth behind the glamour,” *J. Phys. G* **29**, 2343 (2003) [arXiv:hep-ph/0304226].
- [23] M. M. Nojiri, G. Polesello and D. R. Tovey, “Proposal for a new reconstruction technique for SUSY processes at the LHC,” arXiv:hep-ph/0312317.
- [24] Christopher Gorham Lester, *Model independent sparticle mass measurements at ATLAS*, A dissertation submitted to the University of Cambridge for the degree of Doctor of Philosophy December 2001.
- [25] K. Kawagoe, M. M. Nojiri and G. Polesello, “A new SUSY mass reconstruction method at the CERN LHC,” *Phys. Rev. D* **71**, 035008 (2005) [arXiv:hep-ph/0410160].
- [26] B. K. Gjelsten, D. J. Miller and P. Osland, “Measurement of SUSY masses via cascade decays for SPS 1a,” *JHEP* **0412**, 003 (2004) [arXiv:hep-ph/0410303].
- [27] B. K. Gjelsten, D. J. Miller and P. Osland, “Measurement of the gluino mass via cascade decays for SPS 1a,” *JHEP* **0506**, 015 (2005) [arXiv:hep-ph/0501033].
- [28] A. Birkedal, R. C. Group and K. Matchev, “Slepton mass measurements at the LHC,” *In the Proceedings of 2005 International Linear Collider Workshop (LCWS 2005), Stanford, California, 18-22 Mar 2005, pp 0210* [arXiv:hep-ph/0507002].
- [29] C. G. Lester, M. A. Parker and M. J. . White, “Determining SUSY model parameters and masses at the LHC using cross-sections, kinematic edges and other observables,” *JHEP* **0601**, 080 (2006) [arXiv:hep-ph/0508143].
- [30] D. J. Miller, P. Osland and A. R. Raklev, “Invariant mass distributions in cascade decays,” *JHEP* **0603**, 034 (2006) [arXiv:hep-ph/0510356].
- [31] P. Meade and M. Reece, “Top partners at the LHC: Spin and mass measurement,” *Phys. Rev. D* **74**, 015010 (2006) [arXiv:hep-ph/0601124].
- [32] C. G. Lester, “Constrained invariant mass distributions in cascade decays: The shape of the ‘ $m(q\bar{q})$ -threshold’ and similar distributions,” *Phys. Lett. B* **655**, 39 (2007) [arXiv:hep-ph/0603171].
- [33] C. G. Lester, M. A. Parker and M. J. . White, “Three body kinematic endpoints in SUSY models with non-universal Higgs masses,” *JHEP* **0710** (2007) 051 [arXiv:hep-ph/0609298].
- [34] B. K. Gjelsten, D. J. Miller, P. Osland and A. R. Raklev, “Mass determination in cascade decays using shape formulas,” *AIP Conf. Proc.* **903**, 257 (2007) [arXiv:hep-ph/0611259].
- [35] S. Matsumoto, M. M. Nojiri and D. Nomura, “Hunting for the top partner in the littlest Higgs model with T-parity at the LHC,” *Phys. Rev. D* **75**, 055006 (2007) [arXiv:hep-ph/0612249].

[36] H. C. Cheng, J. F. Gunion, Z. Han, G. Marandella and B. McElrath, “Mass Determination in SUSY-like Events with Missing Energy,” *JHEP* **0712**, 076 (2007) [arXiv:0707.0030 [hep-ph]].

[37] C. Lester and A. Barr, “MTGEN : Mass scale measurements in pair-production at colliders,” *JHEP* **0712**, 102 (2007) [arXiv:0708.1028 [hep-ph]].

[38] W. S. Cho, K. Choi, Y. G. Kim and C. B. Park, “Gluino Stransverse Mass,” *Phys. Rev. Lett.* **100**, 171801 (2008) [arXiv:0709.0288 [hep-ph]].

[39] B. Gripaios, “Transverse Observables and Mass Determination at Hadron Colliders,” *JHEP* **0802**, 053 (2008) [arXiv:0709.2740 [hep-ph]].

[40] A. J. Barr, B. Gripaios and C. G. Lester, “Weighing Wimps with Kinks at Colliders: Invisible Particle Mass Measurements from Endpoints,” *JHEP* **0802**, 014 (2008) [arXiv:0711.4008 [hep-ph]].

[41] W. S. Cho, K. Choi, Y. G. Kim and C. B. Park, “Measuring superparticle masses at hadron collider using the transverse mass kink,” *JHEP* **0802**, 035 (2008) [arXiv:0711.4526 [hep-ph]].

[42] G. G. Ross and M. Serna, “Mass Determination of New States at Hadron Colliders,” *Phys. Lett. B* **665**, 212 (2008) [arXiv:0712.0943 [hep-ph]].

[43] M. M. Nojiri, G. Polesello and D. R. Tovey, “A hybrid method for determining SUSY particle masses at the LHC with fully identified cascade decays,” *JHEP* **0805**, 014 (2008) [arXiv:0712.2718 [hep-ph]].

[44] P. Huang, N. Kersting and H. H. Yang, “Hidden Thresholds: A Technique for Reconstructing New Physics Masses at Hadron Colliders,” arXiv:0802.0022 [hep-ph].

[45] M. M. Nojiri, Y. Shimizu, S. Okada and K. Kawagoe, “Inclusive transverse mass analysis for squark and gluino mass determination,” *JHEP* **0806**, 035 (2008) [arXiv:0802.2412 [hep-ph]].

[46] D. R. Tovey, “On measuring the masses of pair-produced semi-invisibly decaying particles at hadron colliders,” *JHEP* **0804**, 034 (2008) [arXiv:0802.2879 [hep-ph]].

[47] M. M. Nojiri and M. Takeuchi, “Study of the top reconstruction in top-partner events at the LHC,” arXiv:0802.4142 [hep-ph].

[48] H. C. Cheng, D. Engelhardt, J. F. Gunion, Z. Han and B. McElrath, “Accurate Mass Determinations in Decay Chains with Missing Energy,” *Phys. Rev. Lett.* **100**, 252001 (2008) [arXiv:0802.4290 [hep-ph]].

[49] W. S. Cho, K. Choi, Y. G. Kim and C. B. Park, “Measuring the top quark mass with m_{T2} at the LHC,” *Phys. Rev. D* **78**, 034019 (2008) [arXiv:0804.2185 [hep-ph]].

[50] M. Serna, “A short comparison between m_{T2} and m_{CT} ,” *JHEP* **0806**, 004 (2008) [arXiv:0804.3344 [hep-ph]].

[51] M. Bisset, R. Lu and N. Kersting, “Improving SUSY Spectrum Determinations at the LHC with Wedgebox and Hidden Threshold Techniques,” arXiv:0806.2492 [hep-ph].

[52] A. J. Barr, G. G. Ross and M. Serna, “The Precision Determination of Invisible-Particle Masses at the LHC,” arXiv:0806.3224 [hep-ph].

[53] N. Kersting, “On Measuring Split-SUSY Gaugino Masses at the LHC,” arXiv:0806.4238 [hep-ph].

- [54] M. M. Nojiri, K. Sakurai, Y. Shimizu and M. Takeuchi, “Handling jets + missing E_T channel using inclusive mT2,” arXiv:0808.1094 [hep-ph].
- [55] H. C. Cheng and Z. Han, “Minimal Kinematic Constraints and M_{T2} ,” arXiv:0810.5178 [hep-ph].
- [56] M. Burns, K. Kong, K. T. Matchev and M. Park, “Using Subsystem M_{T2} for Complete Mass Determinations in Decay Chains with Missing Energy at Hadron Colliders,” arXiv:0810.5576 [hep-ph].
- [57] A. J. Barr, A. Pinder and M. Serna, “Precision Determination of Invisible-Particle Masses at the CERN LHC: II,” arXiv:0811.2138 [hep-ph].
- [58] P. Konar, K. Kong and K. T. Matchev, “ \sqrt{s}_{min} : a global inclusive variable for determining the mass scale of new physics in events with missing energy at hadron colliders,” arXiv:0812.1042 [hep-ph].
- [59] A. J. Barr, “Using lepton charge asymmetry to investigate the spin of supersymmetric particles at the LHC,” Phys. Lett. B **596**, 205 (2004) [arXiv:hep-ph/0405052].
- [60] M. Battaglia, A. Datta, A. De Roeck, K. Kong and K. T. Matchev, “Contrasting supersymmetry and universal extra dimensions at the CLIC multi-TeV e+ e- collider,” JHEP **0507**, 033 (2005) [arXiv:hep-ph/0502041].
- [61] J. M. Smillie and B. R. Webber, “Distinguishing spins in supersymmetric and universal extra dimension models at the Large Hadron Collider,” JHEP **0510**, 069 (2005) [arXiv:hep-ph/0507170].
- [62] M. Battaglia, A. K. Datta, A. De Roeck, K. Kong and K. T. Matchev, “Contrasting supersymmetry and universal extra dimensions at colliders,” *In the Proceedings of 2005 International Linear Collider Workshop (LCWS 2005), Stanford, California, 18-22 Mar 2005, pp 0302* [arXiv:hep-ph/0507284].
- [63] A. Datta, K. Kong and K. T. Matchev, “Discrimination of supersymmetry and universal extra dimensions at hadron colliders,” Phys. Rev. D **72**, 096006 (2005) [Erratum-ibid. D **72**, 119901 (2005)] [arXiv:hep-ph/0509246].
- [64] A. Datta, G. L. Kane and M. Toharia, “Is it SUSY?,” arXiv:hep-ph/0510204.
- [65] A. J. Barr, “Measuring slepton spin at the LHC,” JHEP **0602**, 042 (2006) [arXiv:hep-ph/0511115].
- [66] A. Alves, O. Eboli and T. Plehn, “It’s a gluino,” Phys. Rev. D **74**, 095010 (2006) [arXiv:hep-ph/0605067].
- [67] C. Athanasiou, C. G. Lester, J. M. Smillie and B. R. Webber, “Distinguishing spins in decay chains at the Large Hadron Collider,” JHEP **0608**, 055 (2006) [arXiv:hep-ph/0605286].
- [68] L. T. Wang and I. Yavin, “Spin Measurements in Cascade Decays at the LHC,” JHEP **0704**, 032 (2007) [arXiv:hep-ph/0605296].
- [69] C. Athanasiou, C. G. Lester, J. M. Smillie and B. R. Webber, “Addendum to ‘Distinguishing spins in decay chains at the Large Hadron Collider’,” arXiv:hep-ph/0606212.
- [70] S. Abdullin *et al.* [TeV4LHC Working Group], “Tevatron-for-LHC report: Preparations for discoveries,” arXiv:hep-ph/0608322.

- [71] J. M. Smillie, “Spin Correlations in Decay Chains Involving W Bosons,” *Eur. Phys. J. C* **51**, 933 (2007) [arXiv:hep-ph/0609296].
- [72] K. Kong and K. T. Matchev, “Phenomenology of universal extra dimensions,” *AIP Conf. Proc.* **903**, 451 (2007) [arXiv:hep-ph/0610057].
- [73] C. Kilic, L. T. Wang and I. Yavin, “On the Existence of Angular Correlations in Decays with Heavy Matter Partners,” *JHEP* **0705**, 052 (2007) [arXiv:hep-ph/0703085].
- [74] A. Alves and O. Eboli, “Unravelling the sbottom spin at the CERN LHC,” *Phys. Rev. D* **75**, 115013 (2007) [arXiv:0704.0254 [hep-ph]].
- [75] C. Csaki, J. Heinonen and M. Perelstein, “Testing Gluino Spin with Three-Body Decays,” *JHEP* **0710**, 107 (2007) [arXiv:0707.0014 [hep-ph]].
- [76] A. Datta, P. Dey, S. K. Gupta, B. Mukhopadhyaya and A. Nyffeler, “Distinguishing the Littlest Higgs model with T-parity from supersymmetry at the LHC using trileptons,” *Phys. Lett. B* **659**, 308 (2008) [arXiv:0708.1912 [hep-ph]].
- [77] M. R. Buckley, H. Murayama, W. Klemm and V. Rentala, “Discriminating spin through quantum interference,” arXiv:0711.0364 [hep-ph].
- [78] M. R. Buckley, B. Heinemann, W. Klemm and H. Murayama, “Quantum Interference Effects Among Helicities at LEP-II and Tevatron,” *Phys. Rev. D* **77**, 113017 (2008) [arXiv:0804.0476 [hep-ph]].
- [79] G. L. Kane, A. A. Petrov, J. Shao and L. T. Wang, “Initial determination of the spins of the gluino and squarks at LHC,” arXiv:0805.1397 [hep-ph].
- [80] M. Burns, K. Kong, K. T. Matchev and M. Park, “A General Method for Model-Independent Measurements of Particle Spins, Couplings and Mixing Angles in Cascade Decays with Missing Energy at Hadron Colliders,” *JHEP* **0810**, 081 (2008), arXiv:0808.2472 [hep-ph].
- [81] W. S. Cho, K. Choi, Y. G. Kim and C. B. Park, “ M_{T2} -assisted on-shell reconstruction of missing momenta and its application to spin measurement at the LHC,” arXiv:0810.4853 [hep-ph].
- [82] N. Arkani-Hamed, G. L. Kane, J. Thaler and L. T. Wang, “Supersymmetry and the LHC inverse problem,” *JHEP* **0608**, 070 (2006) [arXiv:hep-ph/0512190].
- [83] B. K. Gjelsten, D. J. Miller and P. Osland, “Resolving ambiguities in mass determinations at future colliders,” *In the Proceedings of 2005 International Linear Collider Workshop (LCWS 2005), Stanford, California, 18-22 Mar 2005, pp 0211* [arXiv:hep-ph/0507232].
- [84] B. K. Gjelsten, D. J. Miller, P. Osland and A. R. Raklev, “Mass ambiguities in cascade decays,” arXiv:hep-ph/0611080.
- [85] M. Burns, *Generalizing the Method of Kinematical Endpoints*, talk given at the Pheno 2008 Symposium “LHC Turn On”, Madison WI, April 28, 2008
- [86] M. Park, *Ambiguities in SUSY mass determination from kinematic endpoints at LHC*, talk given at the Pheno 2008 Symposium “LHC Turn On”, Madison WI, April 28, 2008.
- [87] K. Matchev, *New Physics Signatures and Precision Measurements at the LHC*, talk given at the KITP Conference: “Anticipating Physics at the LHC Collider”, UC Santa Barbara, June 5, 2008.

- [88] Georgia Karapostoli, “Feasibility of SUSY particle mass measurements from endpoints in di-lepton events”, talk given at the CMS SUSY Meeting, December 16 2008, CERN. See also Luc Pape, “Reconstruction of sparticle masses from endpoints (and others) at LHC”, CMS Internal Note CMS IN-2006/12.
- [89] D. Costanzo and D. R. Tovey, “Supersymmetric particle mass measurement with invariant mass correlations,” arXiv:0902.2331 [hep-ph].
- [90] P. Bechtle, K. Desch and P. Wienemann, “Fittino, a program for determining MSSM parameters from collider observables using an iterative method,” *Comput. Phys. Commun.* **174**, 47 (2006) [arXiv:hep-ph/0412012].